© 2020. Published by The Company of Biologists Ltd | Journal of Cell Science (2020) 133, jcs243873. doi:10.1242/jcs.243873

RESEARCH ARTICLE

Cofilin is required for polarization of tension in stress fiber networks during migration

Stacey Lee[1,2] and Sanjay Kumar[1,2,3,*]

ABSTRACT

Cell migration is associated with the establishment of defined leading and trailing edges, which in turn requires polarization of contractile forces. While the actomyosin stress fiber (SF) network plays a critical role in enforcing this polarity, precisely how this asymmetry is established remains unclear. Here, we provide evidence for a model in which the actin-severing protein cofilin (specifically cofilin-1) participates in symmetry breakage by removing low-tension actomyosin filaments during transverse arc assembly. Cofilin knockdown (KD) produces a non-polarized SF architecture that cannot be rescued with chemokines or asymmetric matrix patterns. Whereas cofilin KD increases whole-cell prestress, it decreases prestress within single SFs, implying an accumulation of low-tension SFs. This notion is supported by time-lapse imaging, which reveals weakly contractile and incompletely fused transverse arcs. Confocal and super-resolution imaging further associate this failed fusion with the presence of crosslinker-rich, tropomyosin-devoid nodes at the junctions of multiple transverse arc fragments and dorsal SFs. These results support a model in which cofilin facilitates the formation of high-tension transverse arcs, thereby promoting mechanical asymmetry.

KEY WORDS: Cofilin, Stress fiber, Tension, Front-back polarity, Cell mechanics

INTRODUCTION

Cell migration is critical to many developmental and pathological processes, including wound healing, embryogenesis and cancer progression (Friedl and Gilmour, 2009). Many cells undergo an adhesion-dependent mesenchymal mode of migration, during which cytoskeletal tension is transmitted to the extracellular matrix (ECM) through focal adhesions (Huttenlocher and Horwitz, 2011; Parsons et al., 2010). This migration occurs in several distinct steps, starting with the establishment of front-back polarity, which is driven by a complex set of molecular events involving segregation and activation of proteins including Cdc42, PI3K, Rac and RhoA (Ridley et al., 2003; Vicente-Manzanares et al., 2005). Classically, the Rho GTPases Rac and Cdc42 act through their effectors to stimulate actin polymerization and stabilize lamellipodia and filopodia, respectively (Blanchoin et al., 2014; Ridley et al., 2003). At the rear of the cell, tension is built up through the RhoA-mediated assembly and contraction of actomyosin stress fibers (SFs), which act to stabilize and define the trailing edge. This tension is subsequently released by disassembling or remodeling focal adhesions, leading to trailing edge retraction (Petrie and Yamada, 2012; Vicente-Manzanares et al., 2005). The cycle of leading-edge protrusion, development and transmission of tension, and trailing-edge retraction is repeated during directed mesenchymal migration.

SFs support migration by generating traction forces that drive adhesion formation at the leading edge and adhesion detachment at the trailing edge (Livne and Geiger, 2016; Vicente-Manzanares et al., 2005). The front-back evolution of SFs is highly dynamic, involving assembly from smaller actomyosin subunits, fusion and maturation into thicker filaments, and eventually rupture and disassembly (Cramer et al., 1997; Hotulainen and Lappalainen, 2006; Small et al., 1998). Three SF subtypes can be defined based on their specific localization within the cell and connectivity to focal adhesions (Lee and Kumar, 2016; Small et al., 1998). Toward the leading edge, dorsal SFs, which are connected to one focal adhesion, and transverse arcs, which are not directly connected to focal adhesions, form a physically coupled, interconnected network (Burnette et al., 2014; Lee et al., 2018). As these SFs translocate toward the rear of the cell, transverse arcs often fuse with dorsal SFs flanking the sides of the arc, yielding a ventral SF connected to two adhesions (Hotulainen and Lappalainen, 2006).

Previously, we have shown that each of the SF subtypes plays distinct mechanical roles: dorsal SFs are non-contractile and thus bear little to no intrinsic prestress, transverse arcs are contractile, with the apparent tension depending on the geometry of the connecting SFs, and ventral SFs are highly contractile and can bear high prestresses (Lee et al., 2018). Furthermore, these three SF subtypes are highly interconnected, with transverse arcs forming robust connections with and exerting inward radial forces on non-contractile dorsal SFs. Interestingly, the mechanical properties of an individual SF reflect its assembly history, with SF viscoelastic properties dependent on the degree of incorporation of actin crosslinking proteins (Lee et al., 2018). Our findings hint that the development of mechanical polarity is closely tied to mechanisms of SF assembly. The coupling of mechanics to assembly history may be particularly important at the front of the cell, where SFs are reinforced, fused together or broken down to replenish the G-actin pool for incorporation into new SFs (DesMarais et al., 2005). This dynamic SF turnover is thought to be accompanied by a precisely coordinated generation and release of tension in different regions of the cell (Huttenlocher and Horwitz, 2011; Vicente-Manzanares et al., 2005). For example, epidermal growth factor (EGF)-induced front-back polarization is accompanied by rapid mechanical reinforcement of rear SFs (Kassianidou et al., 2017), suggesting that cells must increase SF prestress and actively remodel the SF network in preparation for migration. However, it remains poorly understood how the contractile activity of multiple SFs across the entire cell is regulated to generate productive polarized migration.

[1]UC Berkeley-UCSF Graduate Program in Bioengineering, USA. [2]UC Berkeley Department of Bioengineering, UC Berkeley, CA, USA. [3]UC Berkeley Department of Chemical and Biomolecular Engineering, 274A Stanley Hall #1762, UC Berkeley, Berkeley, CA 94720-1762, UC Berkeley, CA, USA.

*Author for correspondence (skumar@berkeley.edu)

S.L., 0000-0001-5645-8449; S.K., 0000-0002-9996-4883

Handling Editor: Andrew Ewald
Received 14 January 2020; Accepted 11 May 2020

Journal of Cell Science

Journal of Cell Science (2020) 133, jcs243873. doi:10.1242/jcs.243873

Cofilin is a natural candidate for regulating tension polarization given its critical role in actin turnover. Cofilin-mediated severing of F-actin creates free barbed and pointed ends, both of which may subsequently serve as sites of actin polymerization or depolymerization (Bravo-Cordero et al., 2013; Wioland et al., 2017). However, exactly how cofilin contributes to SF maturation and polarization of tension distribution remains controversial. Some studies have suggested that cofilin is recruited to low-tension SFs. For example, reconstituted actin filaments stressed by optical tweezers or laminar flow bind cofilin in a strongly tension-dependent manner, with tensed filaments resisting cofilin binding and filament severing (Hayakawa et al., 2011; Wioland et al., 2019). Furthermore, in cells, cofilin is enriched along low-tension dorsal SFs, with cofilin depletion producing persistent dorsal SFs that fail to properly fuse with transverse arcs to form ventral SFs (Tojkander et al., 2015). In cells cultured on stretched substrates, cofilin is recruited to SFs upon relaxation of the substrate (Hayakawa et al., 2011). Conversely, significant evidence supports a role for cofilin in preventing excessive SF contractility, with cofilin competing with tropomyosins and non-muscle myosin II (NMMII) for actin binding (DesMarais et al., 2002; Jansen and Goode, 2019; Ono and Ono, 2002). In one such study, cofilin depletion increased myosin light chain (MYL12A and MYL12B; herein denoted MLC) phosphorylation (activation) along SFs, increasing total cell contractility (Wiggan et al., 2012). Cofilin depletion has also been observed to increase nuclear fragmentation, which has been attributed to increased contractile stress on the nucleus (Kanellos et al., 2015; Wiggan et al., 2017). Thus, precisely how cofilin contributes to the development of actomyosin contractility in individual SFs and SF networks remains a major open question.

In this study, we sought to address this controversy by directly investigating the role of cofilin in remodeling and promoting mechanical asymmetry in the SF network. In particular, we test the hypothesis that cofilin is preferentially recruited to low-tension SFs, resulting in deselection of these SFs and promotion of high-tension SFs. We find that cofilin contributes to breaking the symmetry of cellular tension distribution and that cofilin knockdown (KD) attenuates front-back polarity while increasing SF density. While individual SFs in cofilin-depleted cells bear lower tension than SFs in control cells, cofilin KD produces greater whole-cell traction forces. Furthermore, transverse arcs in cofilin-depleted cells fail to fuse together during retrograde flow. Instead, transverse arcs remain thin and form an irregular, poorly contractile network composed of short fragments connected by nodes enriched in α-actinin and devoid of tropomyosin. Impaired front-back polarization cannot be rescued either by introducing chemokines or by culturing cells on asymmetric ECM patterns. Our results therefore support a model in which cofilin breaks mechanical symmetry by removing low-tension SFs or facilitating their fusion with other SFs to form highly contractile SFs.

RESULTS

Cofilin localizes to selected SFs and cofilin KD alters cell morphology

Cofilin severs F-actin and is often found in regions of the cell that are undergoing dynamic actin turnover (e.g. lamellipodia). To investigate cofilin function, we used U2OS osteosarcoma cells, a widely used culture model for cell polarization and migration (Burnette et al., 2014; Hotulainen and Lappalainen, 2006). We found that while a sizeable pool of endogenous cofilin was cytoplasmic and nuclear, cofilin was also commonly found along some dorsal SFs (Fig. 1A, white arrows), and to a lesser extent, along ventral SFs and transverse arcs (Fig. 1A, yellow arrowheads). This variable localization to SFs could reflect differences in SF tensile states and turnover (Hayakawa et al., 2011; Lee et al., 2018; Tojkander et al., 2015).

In order to study the effects of cofilin on actomyosin contractility over different time and length scales, such as during mechanical polarization, we generated stable cell lines depleted of cofilin-1 (cofilin-2 is restricted to skeletal muscle and was therefore not considered here). KD of cofilin-1 resulted in >70% reduction in cofilin-1 and >98% reduction in phosphorylated (inactive) cofilin compared to cells transduced with a control non-targeting (NT) shRNA (P<0.001, Fig. 1B; Fig. S1A). Selective KD of cofilin-1 did not affect expression levels of ADF (also known as DSTN), the other cofilin isoform expressed in non-muscle cells, which is expressed in moderate levels in U2OS cells (Fig. S1B–D). Relative to NT controls, cofilin-1 (hereafter referred to as cofilin) KD cells had markedly different morphologies, with numerous thin SFs distributed in a disorganized manner throughout the cell (Fig. 1C). Furthermore, cofilin KD cells had a higher F-actin:G-actin ratio, consistent with reduced cofilin-severing activity (Fig. S1G). We also observed that the cofilin KD cells were often multinucleated and/or had Hoechst-positive fragments surrounding the nucleus (P<0.001, Fig. 1D). While nuclear fragmentation could suggest decreased nuclear mechanical integrity (Ho and Lammerding, 2012), we did not find changes in the overall expression levels of lamin A/C, the major structural component of the nuclear lamina (Fig. S1E,F), suggesting that the presence of nuclear fragments is not due to an inherent mechanical defect in the nucleus, and could instead be a result of failed cytokinesis (Chen and Pollard, 2011; Hotulainen et al., 2005) or increased mechanical force on the nucleus (Kanellos et al., 2015). Cofilin KD cells also had larger cell spread areas, consistent with aberrant regulation of SF formation and turnover (P<0.01, Fig. 1E). Furthermore, focal adhesions in the cofilin KD cells had a higher average circularity index (P<0.05, Fig. 1F), suggesting that SF-generated forces are less directionally polarized and/or that the associated SFs are exerting lower prestresses. Cofilin KD cells also migrated significantly more slowly than NT controls in random 2D migration assays (P<0.01, Fig. 1G; Movies 1–3). Over the course of the migration assay, cofilin KD cells produced dynamic ruffled edges, but failed to extend the persistent dominant lamellipodia characteristic of a leading edge. These observations are consistent with the reduced directional migration and migration speeds reported in other cell lines (Hotulainen et al., 2005). Finally, rescue of cofilin KD via ectopic expression of EGFP–cofilin eliminated the phenotypic changes brought about by cofilin depletion (Fig. S2). Taken together, these observations suggest that cofilin depletion alters SF turnover, leading to changes in focal adhesion and nuclear morphology and cell migration.

SFs in cofilin KD cells are individually under lower prestress but collectively exert higher traction forces

The thin, disorganized SFs and circular focal adhesion morphology in the cofilin KD cells suggests that these SFs generate lower contractile forces. However, others have reported that depletion of cofilin and ADF results in increased mechanical strain on the nucleus as well as increased phosphorylated MLC localization along SFs (Kanellos et al., 2015; Wiggan et al., 2012, 2017). To quantify how cofilin KD affects cell contractility, we performed traction force microscopy (Fig. 2). Individual U2OS cofilin KD cells exerted higher total traction forces compared to NT control

Journal of Cell Science (2020) 133, jcs243873. doi:10.1242/jcs.243873

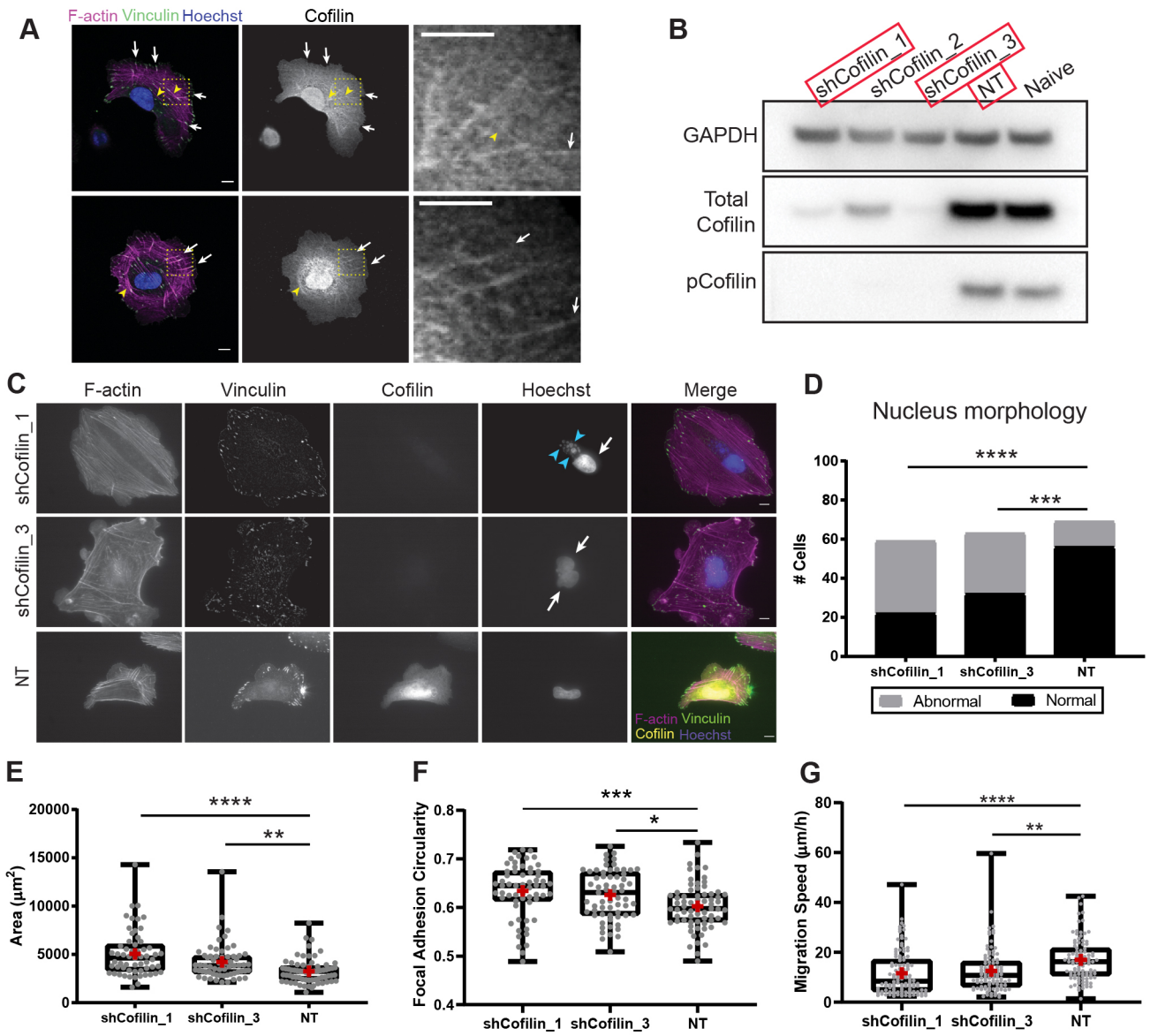

Fig. 1. Cofilin is enriched along dorsal SFs, and cofilin KD cells have altered SF networks and nuclear morphologies. (A) Endogenous cofilin-1 localization in representative U2OS cells. White arrows point to dorsal SFs and yellow arrowheads indicate ventral SFs and transverse arcs. Representative of *n*=44 cells across two independent experiments. (B) Cofilin-1 KD reduces both cofilin and pCofilin expression in U2OS cells. A representative blot from seven independent experiments is shown. Cells transduced with shCofilin_1 and shCofilin_3 shRNA construct variants were used in subsequent experiments. (C) Representative cofilin KD cells stained for F-actin (magenta), cofilin (yellow), vinculin (green) and Hoechst (blue). White arrows point to multiple nuclei within a cell and blue arrowheads point to nuclear fragments. (D) Distribution of cofilin KD cells that contain abnormal nuclei, defined as either being multinucleated and/or containing nuclear fragments ('abnormal' shown in gray). (E) Distribution of projected cell areas for cofilin KD cells and NT controls. (F) Distribution of focal adhesion circularity. Each point represents the average circularity of focal adhesions in one cell. (G) Distribution of random migration speeds. Each point represents the average instantaneous migration speed of a cell calculated over 6 h. See also Movies 1–3. For D–F: *n*=59, 63 and 69 for shCofilin_1, shCofilin_3 and NT cells, respectively, across three independent experiments. For G: *n*=111, 98 and 96 for shCofilin_1, shCofilin_3 and NT cells, respectively, across three independent experiments. Plots in E–G show the 25th, 50th and 75th percentiles, with whiskers extending to the maximum and minimum. The red cross indicates the mean. **P*<0.05, ***P*<0.01, ****P*<0.001, *****P*<0.0001 [χ-squared test (D) or Kruskal–Wallis post-hoc Dunn's test (E–G)]. Scale bars: 10 µm.

cells (*P*<0.01, Fig. 2A,B). When we normalized traction force by projected area (traction stress) cofilin KD cells also generated higher traction stresses (*P*<0.05, Fig. 2C). To determine whether the higher traction forces observed in cofilin KD cells were accompanied by increased tension within individual SFs, we measured SF mechanics using laser nanosurgery (Chang and Kumar, 2013; Kassianidou et al., 2017; Kumar et al., 2006; Lee et al., 2018; Tanner et al., 2010). In this assay, a single SF is photosevered and the resulting ends are tracked as they recoil away from one another. The total distance retracted reflects the elastic energy stored within the SF, with a larger retraction distance indicating more stored energy. To standardize cell shape, area and SF length for these tension measurements, we first cultured cells on fibronectin U-shape patterns in which an SF of a defined length is induced to form across an ECM gap (Kassianidou et al., 2017; Théry et al., 2006b) (Fig. 3A). Next, we severed the SF that spanned the gap of the pattern and tracked its retraction over time (Fig. 3B; Movie 4). We then fitted the retraction of the SF to a Kelvin–Voigt model, which treats the SF as a viscoelastic material comprising a series of parallel springs and dashpots (Kumar et al., 2006; Tanner et al.,

Journal of Cell Science (2020) 133, jcs243873. doi:10.1242/jcs.243873

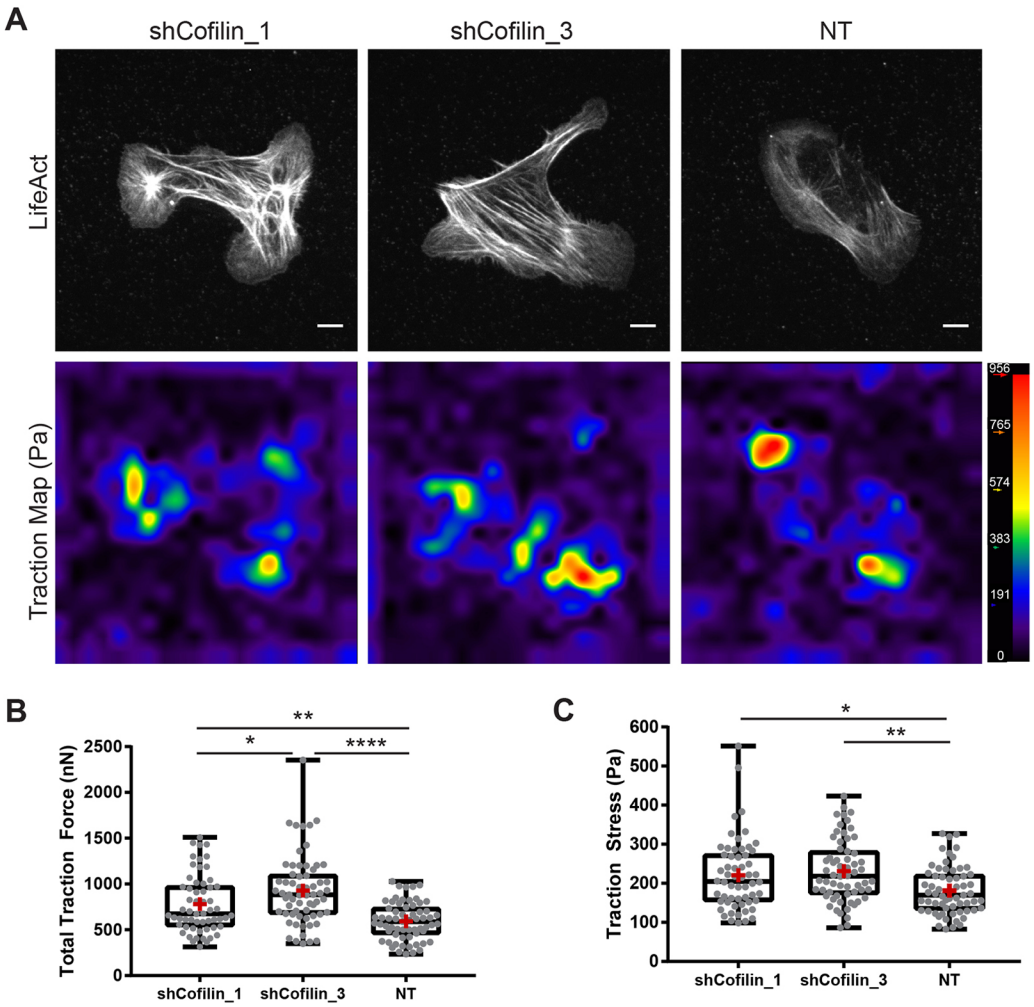

Fig. 2. Cofilin KD cells generate higher traction forces than NT controls. (A) Top panel, representative Lifeact images of cells. Bottom panel, corresponding traction maps. (B) Distribution of total traction forces (traction forces integrated over cell area) exerted by the cells. (C) Distribution of traction stresses (traction force normalized by cell area). *n*=58, 63, and 63 cells for shCofilin_1, shcofilin_3 and NT cells, respectively, from three independent experiments. Boxes show the 25th, 50th and 75th percentiles, with whiskers extending to the maximum and minimum. The red cross indicates the mean. **P*<0.05; ***P*<0.01; *****P*<0.0001 (Kruskal–Wallis test, post-hoc Dunn's test). Scale bars: 10 µm.

2010). From this fitting, the characteristic parameters L_o, the stored elastic prestress of the SF, and τ, the viscoelastic time constant or the ratio of viscosity to elasticity, are derived (Fig. 3C). We found that the median L_o for SFs in the cofilin KD cells was lower than that of the NT controls (P<0.05, Fig. 3D). The lower SF prestresses suggest that cofilin-depleted cells are deficient in generating high tension in individual SFs. The time constants (τ) were not significantly different across cell lines (Fig. 3E). Further characterization of SFs via immunostaining revealed that tropomyosin levels were higher in cofilin-depleted cells (Fig. S3A,C,F). An inverse relationship between cofilin and tropomyosin activity is consistent with observations that cofilin competes with some isoforms of tropomyosin for actin binding (DesMarais et al., 2002; Hsiao et al., 2015; Jansen and Goode, 2019; Ono and Ono, 2002). Interestingly, we did not see cofilin-dependent differences in the localization of doubly phosphorylated (pp)MLC along the ventral SF spanning the gap of the U-pattern, despite the measured differences in SF prestress (Fig. S3A,B,D). This indicates that there may be functionally important differences in cofilin-induced ppMLC organization that are undetectable by diffraction-limited imaging, or that the mechanical effects are not solely regulated by ppMLC levels. Together with the findings from the traction force studies (Fig. 2), these results suggest that cofilin KD cells exert higher traction forces due to an increase in the number of SFs. These SFs individually bear lower tension but collectively exert higher traction forces.

Altered transverse arc morphology in cofilin KD cells impairs fusion of adjacent SFs

Immunofluorescence imaging (Fig. 1), traction force microscopy (Fig. 2) and SF ablation measurements (Fig. 3) suggest that cofilin KD cells accumulate low-tension SFs. Additionally, random migration assays revealed that cofilin KD cells were largely unable to maintain a persistent leading edge and migrated with lower speeds (Fig. 1G). We were thus motivated to examine how cofilin depletion would impact SF morphodynamics, which led us to conduct time-lapse imaging of RFP–Lifeact-transduced cells as they spread and migrated along an unpatterned fibronectin-coated glass surface. In NT control cells, transverse arcs formed smoothly curved SFs that spanned the lamella as a continuous structure (Fig. 4A, top panel). Over time, these transverse arcs moved toward the back of the cell and often fused together with adjacent transverse

Journal of Cell Science (2020) 133, jcs243873. doi:10.1242/jcs.243873

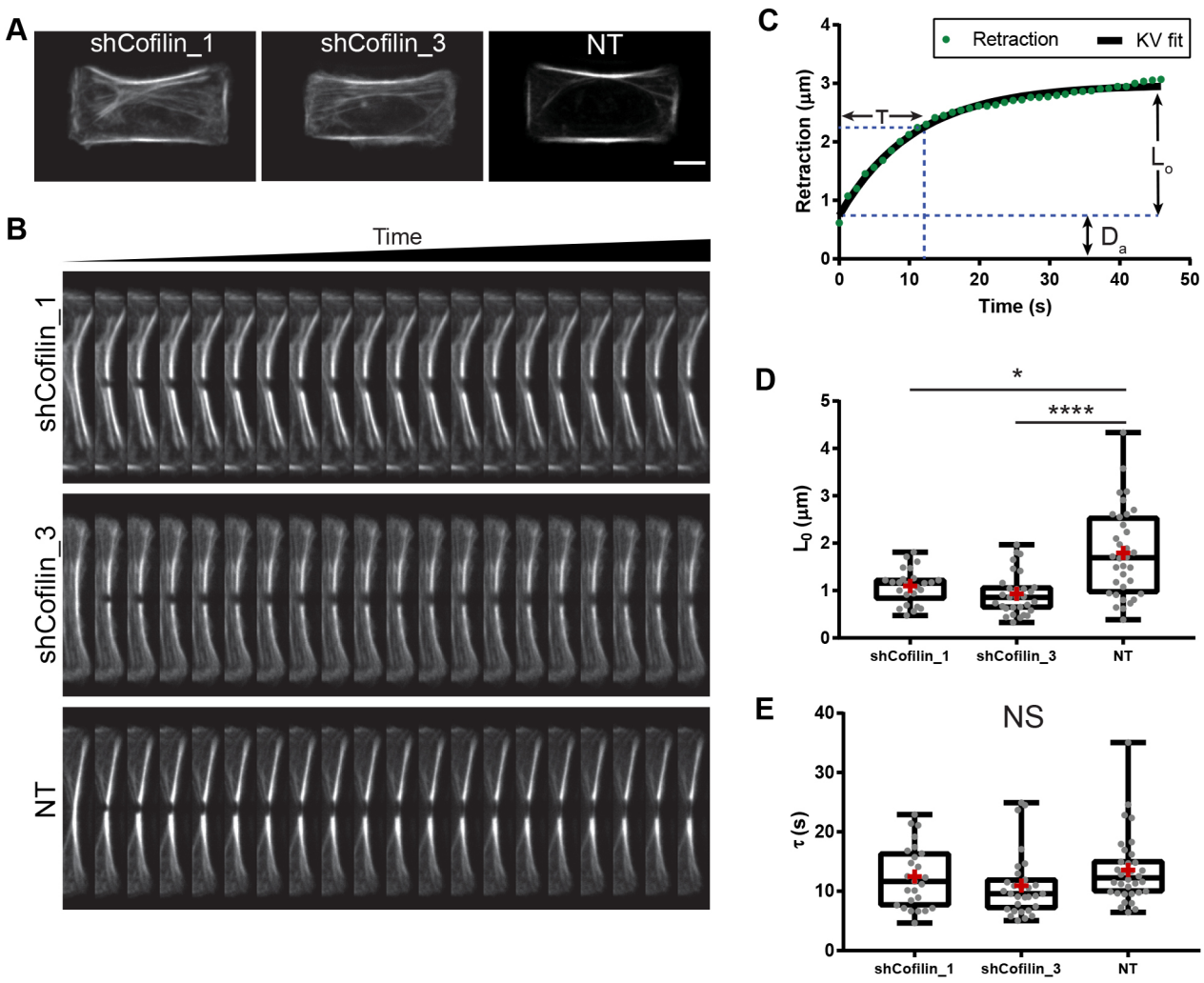

Fig. 3. Single SFs in cofilin KD cells exert lower prestresses. (A) Representative images of U2OS cells patterned onto U-patterns. The SF spanning the gap of the U-pattern was severed. (B) Kymographs of the severed SF. The time between slices is 2.5 s with a total time of 50 s. See also Movie 4. (C) Example SF retraction trace tracked over time. Retraction at time *t* is defined as the half-distance between the severed ends. SF retraction is fitted to the Kelvin–Voigt model. Characteristic parameters L_o (elastic prestress), τ (viscoelasticity) and D_a (length of SF destroyed during ablation) are derived from the fitting (see Materials and Methods). (D) Distribution of fitted L_o prestresses. (E) Distribution of viscoelastic time constants. *n*=25, 30 and 34 for shCofilin_1, shCofilin_3 and NT cells, respectively, across six or seven independent experiments. Boxes show the 25th, 50th and 75th percentiles, with whiskers extending to the maximum and minimum. The red cross indicates the mean. **P*<0.05; *****P*<0.0001; NS, not significant (Kruskal–Wallis test, post-hoc Dunn's test). Scale bar: 10 µm.

arcs to form thicker SFs (Fig. 4A, bottom; Movie 5). In contrast, many cofilin KD cells contained transverse arcs that were jagged and discontinuous, and failed to span the entire lamella as a unit (*P*<0.01, Fig. 4A,B). These transverse arcs made up a geodesic nodal network, formed when a population of disorganized, short SFs in areas of active actin polymerization and membrane protrusion, aggregated together to form aster-like nodes (Fig. 4C–E, blue and green arrowheads). The nodes extended to and bridged adjacent arcs and dorsal SFs, preventing SF fusion during their translocation toward the cell center (Fig. 4A, bottom panel, 4E blue and green arrowheads; Movies 6 and 7). In contrast, few NT cells displayed permanent nodal SF morphologies. The lamellar SF network in NT cells had a greater degree of organization and alignment, with SFs orienting roughly parallel to one another and the leading edge. As SFs flowed toward the back of the cell, these fragments coalesced into cohesive transverse arcs spanning the width of the lamella. While some NT cells displayed nodes during SF movement, the nodes were absorbed into normal dorsal SF-transverse arc connections as a subset of filaments attached to the node were depolymerized or reorganized into the arc (Fig. 4E, purple and magenta arrowheads; Movies 8 and 9). These results suggest that the nodes are transient, intermediate structures in the SF network of naïve cells, but persist in cofilin-depleted cells where they act as physical barriers to the fusion of adjacent transverse arcs.

Interestingly, we found these nodes to be rich in the actin-binding crosslinking proteins α-actinin and filamin, which are known to bridge adjacent F-actin filaments and maintain cohesive SF bundles. Using structured illumination microscopy (SIM) and confocal imaging, we found that, in NT cells, α-actinin localized continuously along dorsal SFs, and periodically along transverse arcs and ventral SFs, with bands spaced ∼1.5 µm apart (Fig. 4C; Fig. S4A–C, white arrows). Similarly, in cofilin-depleted cells, α-actinin localization along dorsal and ventral SFs was continuous and periodic, respectively. However, while α-actinin displayed some normal banding patterns along the transverse arcs in the cofilin-depleted cells, α-actinin also assembled into large clusters at the nodes (Fig. 4C; Fig. S4A–C, blue arrowheads). The fluorescence intensity of α-actinin at these nodes was as high as three times the

Journal of Cell Science (2020) 133, jcs243873. doi:10.1242/jcs.243873

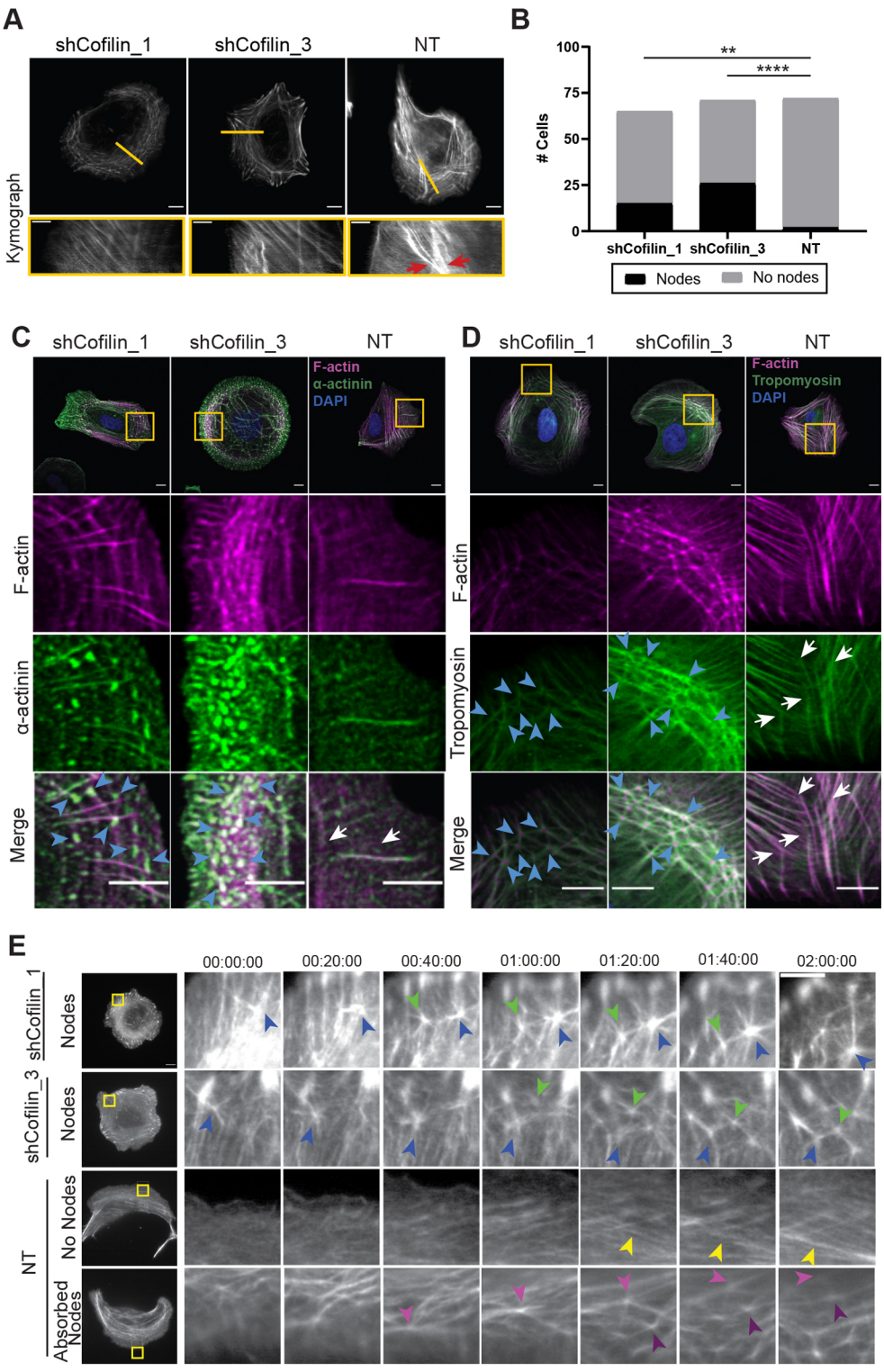

Fig. 4. Transverse arcs in cofilin KD cells have altered morphodynamics. (A) Still images (top panel) and kymographs derived from line scans drawn perpendicular to a dynamic edge to track retrograde transverse arc movement (bottom panel) in representative cells. The yellow line indicates the position of the line scan used to generate the kymograph. Kymographs show movement of transverse arcs toward the cell center. Red arrows point to sites of transverse arc fusion. Scale bars: 10 µm (top), 5 µm (bottom panel kymograph). Cells were tracked for a total of 135 minutes. Time between slices is 1 minute.. SFs are tagged with RFP-Lifeact. Representative cells are shown. *n*=47, 24 and 41 for shCofilin_1, shCofilin_3 and NT cells, respectively, imaged across three, two and three independent experiments. See also Movie 5. (B) Distribution of cells displaying nodal morphologies. ***P*<0.01, *****P*<0.0001 (χ-squared test). *n*=65, 71 and 72 for shCofilin_1, shCofilin_3 and NT cells, respectively, across three independent experiments. (C,D) Confocal images of cells stained for F-actin (magenta), DAPI (blue), and (C) α-actinin (green) or (D) tropomyosin (green). Blue arrowheads point to nodal intersections. White arrows point to transverse arc-dorsal SF intersections in NT cells. Scale bars: 10 µm. See also Fig. S4. For C, representative cells are shown from a sample size of *n*=27, 28 and 26 for shCofilin_1, shCofilin_3, and NT cells, respectively, across two independent experiments. For D, representative images are shown from a sample size of *n*=31, 31 and 30 for shCofilin_1, shCofilin_3 and NT cells, respectively, across two independent experiments. Scale bars: 10 µm. (E) Node formation and tracking in cofilin KD and NT cells. Yellow boxes indicate regions enlarged in time series panel. Blue and green arrowheads indicate examples of persistent nodes that form and translocate toward the cell center. Yellow arrowheads indicate annealing and fusion of short SF fragments into transverse arcs. Magenta and purple arrowheads track examples of nodes that form and resorb into transverse arcs. Scale bars: 10 µm. Time is given as HH:MM:SS. Representative images are shown. *n*=56, 45 and 47 for shCofilin_1, shCofilin_3 and NT cells, respectively, imaged across three independent experiments. See also Movies 6–9.

fluorescence intensity of α-actinin along transverse arcs in comparable regions in NT cells (Fig. S4B). These nodes were also enriched in the crosslinking protein filamin A (Fig. S5A), which has been implicated in the reinforcement of F-actin filaments joined together at large angles (Nakamura et al., 2011).

Transverse arcs have been observed to form from the annealing of Arp2/3-nucleated actin branches with myosin/tropomyosin complexes (Tojkander et al., 2011). This mechanism may reflect a balance between Arp2/3-driven polymerization, which supplies actin and crosslinking proteins, and myosin/tropomyosin activity, which confers contractile function. Furthermore, in branched actin networks, cofilin has been found to sever actin at Arp2/3-nucleated branches (Blanchoin et al., 2000; Chan et al., 2009). This debranching creates free barbed ends, which subsequently allows tropomyosin to bind to the severed filaments (Hsiao et al., 2015). Tropomyosin binding prevents further cofilin-mediated severing,

Journal of Cell Science (2020) 133, jcs243873. doi:10.1242/jcs.243873

facilitating the formation of a stable contractile SF. This process may be important in the transition from a highly-branched, dendritic network in the lamellipodium to more linear, organized transverse arc SFs in the lamella during retrograde flow. To test whether the nodes in the cofilin-depleted cells resulted from an alteration in polymerization/contractility balance, we next examined tropomyosin and Arp2/3 complex localization. Mature individual SFs in cofilin-depleted cells contained higher levels of tropomyosin (Fig. S3A,C), consistent with previous findings that cofilin and tropomyosin competitively bind to actin (Hsiao et al., 2015; Ono and Ono, 2002). However, we found that nodes in transverse arcs, which are less mature SFs compared to ventral SFs, were specifically devoid of tropomyosin (Fig. 4D; Fig. S4D, blue arrowheads). Furthermore, line scans in these nodal regions exhibited large variations in tropomyosin fluorescence intensity (Fig. S4E). In contrast, transverse arcs in NT cells had mostly continuous tropomyosin decoration, with minimal variation in fluorescence intensity (Fig. 4D; Fig. S4D,E, white arrows). The nodes, when present, were also enriched in Arp3 and filamin (Fig. S5), suggesting aberrant SF branching or crosslinking. The lack of overlap between tropomyosin and α-actinin in nodes of geodesic actin networks has been previously reported in spreading cells prior to the establishment of a mature SF network (Lazarides, 1976). These observations are consistent with the idea that cofilin depletion favors the accumulation of branched actin filaments and their eventual incorporation into a highly interconnected transverse arc network, at the expense of forming organized, productively contractile transverse arcs in the lamella.

Both the hyper-connected geodesic dome-like geometry of the transverse arc network and a lack of tropomyosin at the nodes in the cofilin-depleted cells led us to hypothesize that these nodal arrangements were globally less contractile than arc networks in NT cells. We arrived at this hypothesis for two reasons. First, connected SFs can broadly distribute forces over SF networks (Chang and Kumar, 2013; Kassianidou et al., 2017; Kumar et al., 2019), suggesting that nodal transverse arcs cannot concentrate tension in individual SFs. Second, tropomyosin facilitates NMMII binding to actin and is needed for proper arc assembly (Tojkander et al., 2011). To test this hypothesis, we first examined the localization of ppMLC, which indicates active (contractile) NMMII, and found that that the nodal regions in transverse arcs were also devoid of ppMLC (Fig. 5A,B, blue arrowheads). Next, we severed transverse arcs in cofilin KD and NT cells to measure tension (Fig. 5C). We found that transverse arcs in the cofilin KD cells were under lower prestress than those in NT controls (P<0.05, Fig. 5D). This finding suggests that individual SFs fail to generate large prestresses, which in turn might affect cell shape. For example, a reduction in transverse arc contractility could prevent transverse arcs from levering down on orthogonally connected dorsal SFs, thereby inhibiting lamellar flattening (Burnette et al., 2014). Indeed, when we obtained z-stacks and measured cell height by taking the distance from the bottom plane of the cell to the top of the nucleus, we found that cofilin KD cells had greater cell heights than NT controls (P<0.05, Fig. 5E,F).

Cofilin depletion reduces cell polarization

Lamellar flattening is one of the hallmarks of mesenchymal cell migration (Burnette et al., 2014). Therefore, the greater cell heights in cofilin KD cells could suggest deficiencies in generating a stable leading edge. Supporting this notion, the majority of NT cells exhibited polarized shapes and SF architectures as defined by a dominant fan-shaped leading edge containing transverse arcs orthogonally intersecting with dorsal SFs, as well as pointed trailing edges containing ventral SFs (Fig. 6A,B). In contrast, a significant majority of the cofilin KD cells were non-polarized, as characterized by rounded morphologies often accompanied by fragmented, circumferential transverse arcs and multiple small protrusions distributed around the cell (P<0.0001, Fig. 6B,E, blue bars). This finding is consistent with previous studies reporting deficiencies in polarization upon cofilin depletion (DesMarais et al., 2004; Hotulainen et al., 2005).

All of the above studies were conducted in the absence of a strong migratory stimulus, such as a chemokine. To ask whether introduction of a chemokine could overcome the loss of cofilin and rescue polarity, we conducted time-lapse imaging of cells on fibronectin-coated surfaces and treated with 100 ng/ml EGF, which we have previously shown to induce polarization (Kassianidou et al., 2017). In NT cells, EGF induced membrane ruffling, with a majority of the cells exhibiting a polarized SF morphology 4 h after EGF addition (Fig. 6C,E, magenta bars; Movie 10). In contrast, a significantly higher number of the cofilin KD cells failed to polarize 4 h after EGF addition (P<0.0001, Fig. 6C,E, magenta bars; Movie 10). Many of the cells either remained rounded, with transverse arcs or ventral SFs ringing the cell, or developed multiple dynamic protrusions. We also seeded cells on adhesive crossbow micropatterns (Fig. 6D), which have been used in the past to impose a polarized SF arrangement in cells (Lee et al., 2018; Thery et al., 2006a; Théry et al., 2006b). We found that 65% of the NT cells assessed formed transverse arcs and dorsal SFs in the curved region of the crossbow, indicating that their SFs were arranged in the expected configuration (Fig. 6E, green bars). In contrast, a much smaller number of the cofilin KD cells took on the expected polarized SF arrangement; cells either formed transverse arcs and dorsal SFs in regions beyond the arc or did not develop these structures at all (P<0.0001, Fig. 6D,E, green bars).

Finally, we asked whether ectopic expression of cofilin could rescue the mechanical polarity defects in the cofilin KD cells. To do so, we transfected cells with a wild-type cofilin (EGFP–Cofilin_WT) or a constitutively active (non-phosphorylatable) cofilin mutant (EGFP–Cofilin_S3A) expression plasmid (Lai et al., 2008; Mannherz et al., 2005). Cofilin KD cells transfected with the WT cofilin construct displayed polarized SF architectures that resembled both transfected and non-transfected NT cells (Fig. S2E). Transfection with cofilin_S3A resulted in similar phenotypes. Conversely, cofilin KD cells transfected with a dominant-negative (phosphomimetic) cofilin mutant (EGFP–Cofilin_S3D) retained an unpolarized morphology, often with nodal SF networks (Fig. S6A). Additionally, many NT control cells transfected with the dominant-negative cofilin were not polarized and displayed instances of nodal networks (Fig. S6B). Taken together, these results suggest that cofilin is needed for mechanical polarization of the SF network.

DISCUSSION

While cofilin has long been established to contribute to polarization and persistent migration, the mechanism has remained unclear. Previous studies have suggested that cofilin can either promote (Hayakawa et al., 2011; Tojkander et al., 2015) or prevent excessive (Kanellos et al., 2015; Wiggan et al., 2012, 2017) SF tension, the former by deselecting low-tension SFs and the latter by reducing myosin binding to SFs. Our study begins to clarify this mixed picture through direct measurements of SF assembly and mechanics in the setting of cofilin depletion. We find that cofilin KD results in an accumulation of SFs that reduces tension within individual SFs

Journal of Cell Science (2020) 133, jcs243873. doi:10.1242/jcs.243873

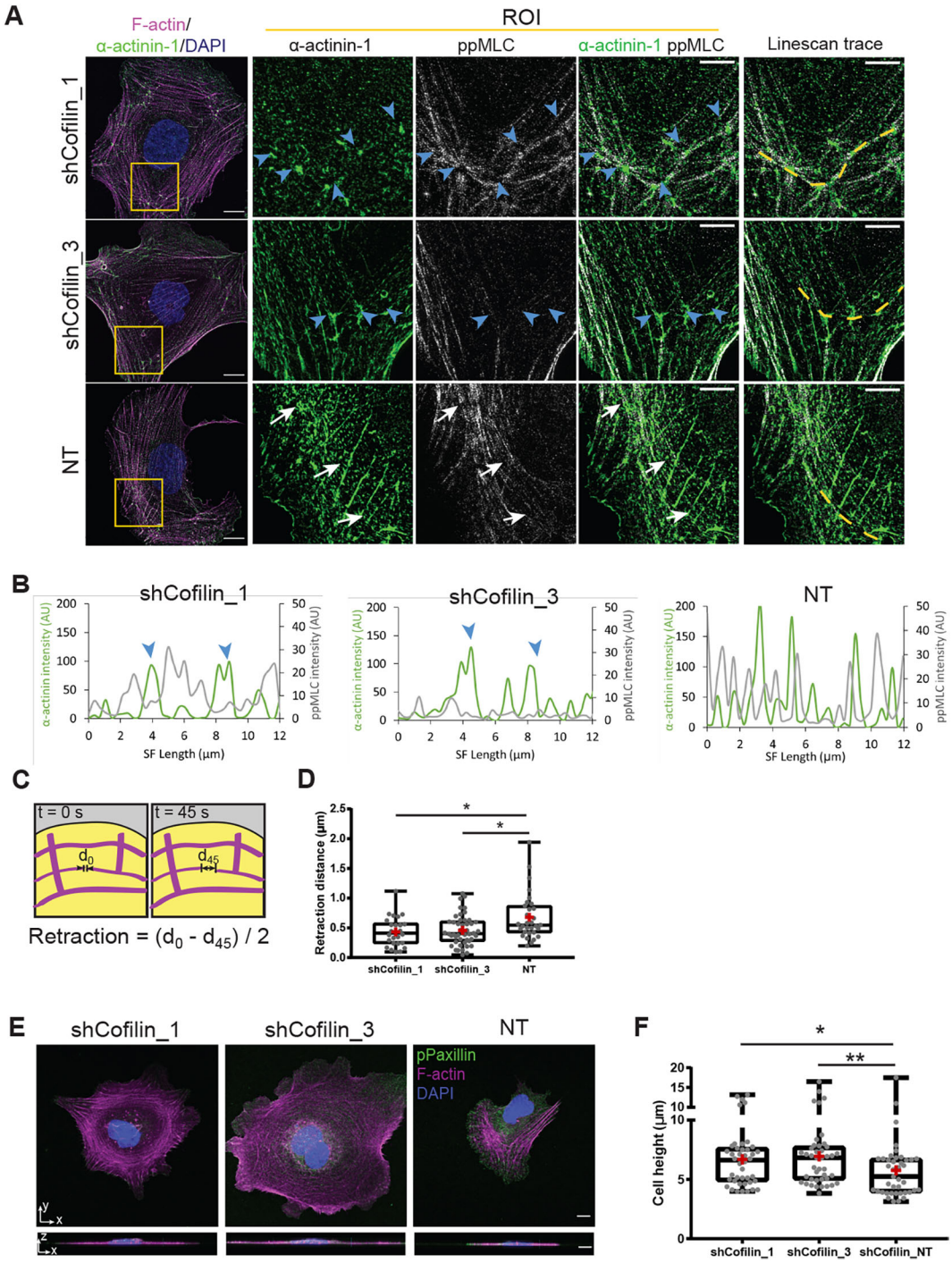

Fig. 5. Transverse arcs in cofilin KD cells generate lower contractile forces. (A) SIM images of U2OS cells stained for α-actinin and ppMLC. Blue arrowheads point to α-actinin clusters and white arrows point to smaller, periodic α-actinin bands. Scale bars: 10 µm (left), 5 µm (ROI panels). Magenta, F-actin; green, α-actinin; white, ppMLC; blue, DAPI. *n*=3 cells per condition across one independent experiment. (B) Line scans along transverse arcs (indicated by the dashed yellow line in A) in the ppMLC (gray) and α-actinin (green) channels. Blue arrowheads indicate nodal regions devoid of ppMLC. (C) Schematic of transverse arc retraction measurement and calculation. (D) Distribution of transverse arc prestresses in cofilin KD and NT cells. *n*=26, 46 and 31 transverse arcs, each from different shCofilin_1, shCofilin_3 and NT cells, across three or four independent experiments. (E) Top panel: basal plane of cells stained for F-actin (magenta), pPaxillin (green) and DAPI (blue). Bottom panel: Z-stack reconstructions of cofilin KD and NT cells. Scale bars: 10 µm. (F) Distribution of nuclear heights in cofilin KD and NT cells. *n*=42, 42 and 41 shCofilin_1, shCofilin_3 and NT cells, respectively, across three independent experiments. Boxes in D and F show the 25th, 50th and 75th percentiles, with whiskers extending to the maximum and minimum. The red cross indicates the mean. **P*<0.05, ***P*<0.01 (Kruskal–Wallis, post-hoc Dunn's test).

but increases traction forces in the whole cell. Moreover, cofilin is particularly important in the formation of transverse arcs and their subsequent fusion into thicker arcs and into ventral SFs, both of which can generate higher contractility than their precursor SFs. Our findings implicate cofilin in removing lower-tension short (e.g. formin-nucleated) and/or branched (e.g. Arp2/3-nucleated)

Journal of Cell Science

Journal of Cell Science (2020) 133, jcs243873. doi:10.1242/jcs.243873

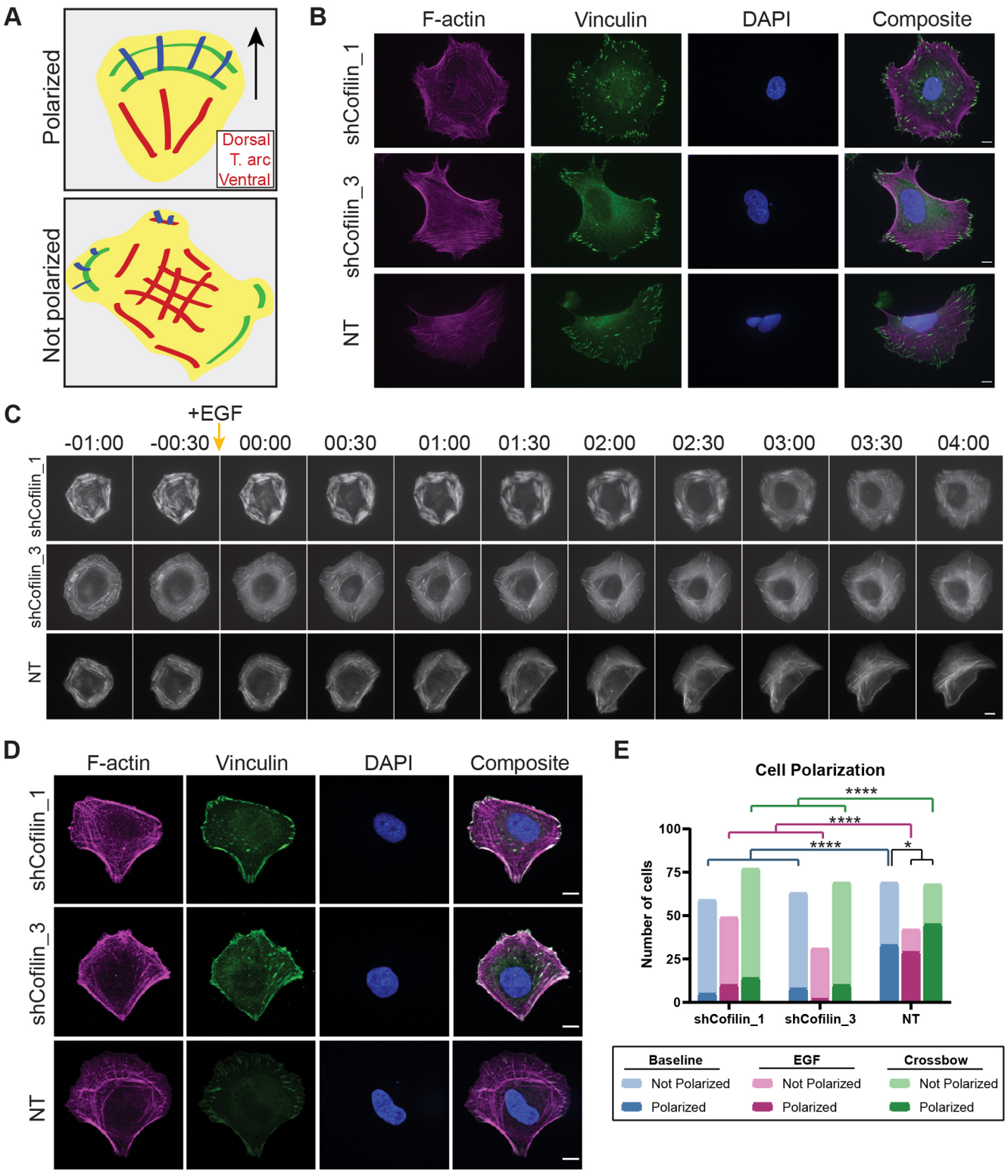

Fig. 6. Cofilin KD cells do not form a polarized SF architecture. (A) Schematic of polarized cells (top) and non-polarized cells. Dorsal SFs (blue), transverse arcs (green) and ventral SFs (red) have distinct localizations and focal adhesion connections. Black arrow denotes the direction of migration. (B) Confocal images of representative untreated baseline cofilin KD and NT cells stained for vinculin (green), phalloidin (magenta) and DAPI (blue). Scale bars: 10 µm. (C) Series of images depicting representative cofilin KD and NT cells tracked before and after treatment with EGF. SFs are visualized with RFP–Lifeact. See also Movie 10. (D) Confocal images of representative cofilin KD or NT cells patterned on crossbow micropatterns and stained for phalloidin (magenta), vinculin (green) and DAPI (blue). (E) Distribution of polarized and non-polarized baseline (blue bars), EGF-treated (magenta bars), and crossbow-patterned (green bars) for cofilin KD and NT cells. Baseline cells: 59, 63 and 69 for shCofilin_1, shCofilin_3 and NT cells, respectively, across three independent experiments. EGF-treated cells: 49, 31 and 42 for shCofilin_1, shCofilin_3 and NT cells, respectively, across two or three independent experiments. Crossbow-patterned cells: n=77, 69 and 68 for shCofilin_1, shCofilin_3 and NT cells, respectively, across three independent experiments. *P<0.05, ****P<0.0001 (χ squared test, followed by Fisher's exact test for pairwise comparisons). Scale bars: 10 µm.

Journal of Cell Science (2020) 133, jcs243873. doi:10.1242/jcs.243873

actin filaments that are not directly tensed by NMMII during transverse arc assembly (Fig. 7A–C, left). Specifically, cofilin breaks down short actin filaments or debranches actin, which enables the formation of stackable, smoothly continuous arcs that eventually undergo fusion into thicker SFs that generate concentrated, centripetally directed contractile forces (Fig. 7D, left). Small

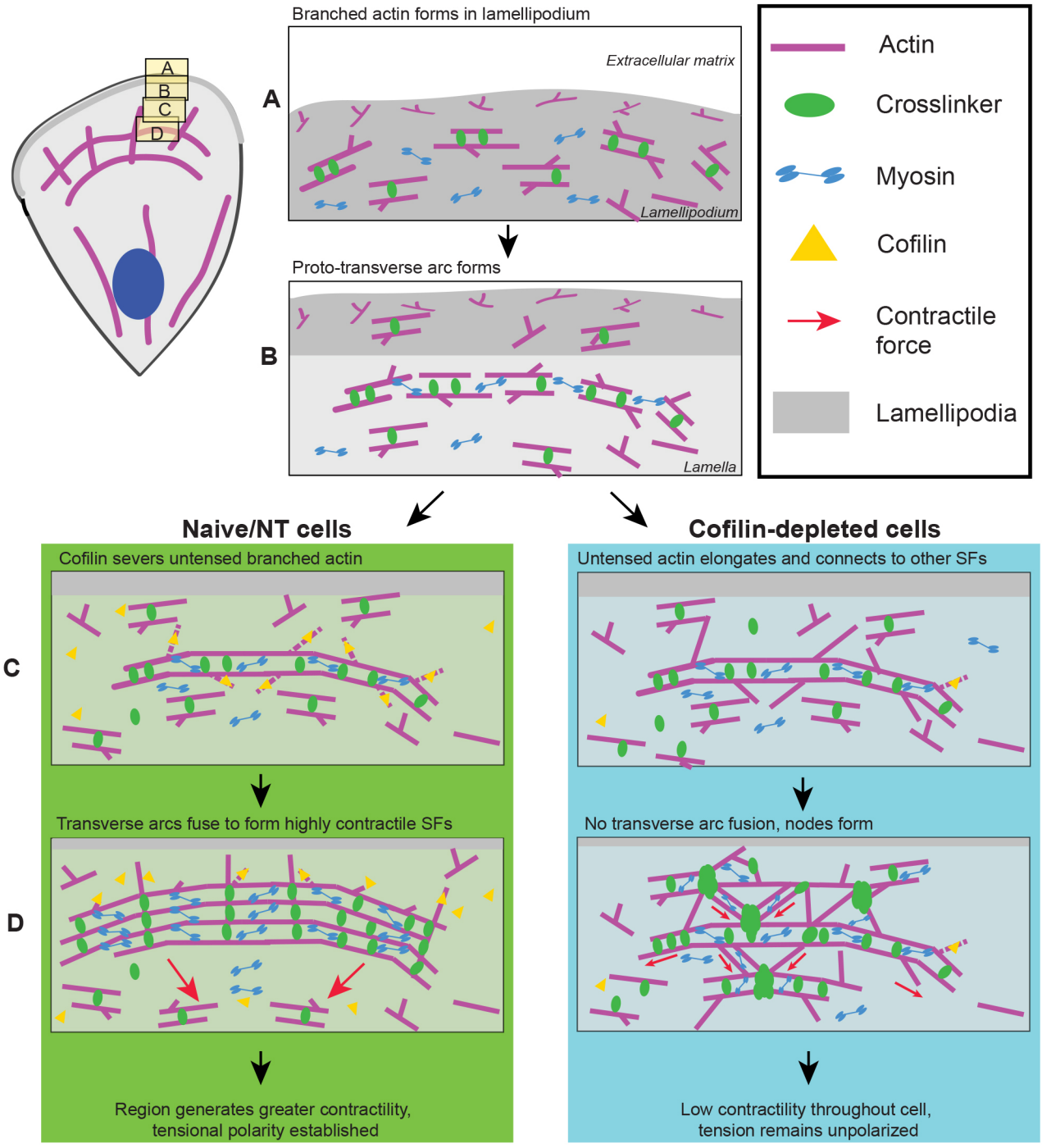

Fig. 7. Cofilin is responsible for front-back polarization of tension distribution through selective removal of low-tension SFs, either by targeting them for disassembly or by participating in the fusion of SFs into higher tension SFs. (A) Short actin fragments are formed in the lamellipodium via Arp2/3 or formin-nucleated processes. (B) Behind the lamellipodium, actin filaments associate with mDia2, tropomyosin and myosin II (blue barbells) fragments which assemble into proto-transverse arcs. (C) Cofilin (yellow triangles) trims excess actin that is not incorporated directly into the transverse arc. In cofilin KD cells, branched actin filaments not incorporated into transverse arcs continue to elongate and form connections with other adjacent transverse arcs. Furthermore, persistent, disorganized F-actin filaments that form from alternative methods (e.g. via formins) might also aggregate into nodes via filamin crosslinking activity. (D) Increasing contractility aligns actomyosin fragments into a smooth arc shape. Cofilin trims excess actin filaments to facilitate the formation of a smooth, contractile arc that may fuse with adjacent transverse arcs to form a thicker, more contractile SF. This, in turn, generates a sufficiently high force to break the tensional symmetry of the cell and leads to tensional polarization. In cofilin-depleted cells, the formation of nodal, crosslinker-rich junctions prevents effective long-range contractile force generation and fusion of adjacent SFs, leading to unproductive force generation and no polarization.

Journal of Cell Science (2020) 133, jcs243873. doi:10.1242/jcs.243873

inhomogeneities in the rate of transverse arc fusion facilitate SF tensional symmetry breaking in the cell, as others have described (Tee et al., 2015). This leads to establishment and reinforcement of a single leading edge and disassembly of arcs in other regions and, eventually, a polarized cell. Conversely, diminished cofilin activity results in the accumulation of short actin filaments and branched actin, both of which can lead to the aggregation of SFs into aster-like points due to crosslinking activity by proteins such as α-actinin and filamin. SFs that make up the nodal network reduce contractility in the lamella of the cell through two mechanisms: first, by acting as incompressible struts to prevent the fusion of neighboring arcs into more contractile SFs and, second, by forming a hyper-connected network that broadly redistributes and disperses tension (Fig. 7C,D, right). An inability to build tension in the lamella, together with an accumulation of discontinuous, low-tension SFs leads to a failure to develop and establish tensional polarity needed for directed migration.

Our findings implicate cofilin in promoting the formation of contractile SFs, as well as in the regulation of overall cell tension and polarization. Depleting cofilin led to the accumulation of weakly contractile SFs and the formation of a geodesic SF network, which may represent a low-tension intermediate SF arrangement (Luo et al., 2013, 2016) that would normally progress into mature arcs but persists in the absence of cofilin. Geodesic actin structures with α-actinin-positive, tropomyosin-negative nodes were first reported several decades ago in non- or incompletely polarized cells and were proposed at the time to serve as SF progenitors (Lazarides, 1976; Osborn et al., 1978). Our findings provide direct support for this idea. As noted earlier, cofilin has also been reported to compete with myosin for actin binding within HeLa cells, with cofilin depletion producing excessive myosin binding and contractility (Wiggan et al., 2012). In that study, cofilin KD was predicted to increase prestress within a single SF, which was corroborated by analysis of SF retraction following spontaneous rupture following latrunculin B treatment. In contrast, we find through laser ablation experiments that cofilin KD reduces single-SF prestress. There are a number of potential explanations for the disagreement between the two studies. First, SFs presumably rupture spontaneously only after building up very high tensile forces, whereas laser ablation does not preselect fibers according to tension. Thus, the two approaches may select for a different subset of SFs. The time needed for latrunculin to sensitize SFs to rupture might introduce further selective effects. Second, differences in cell morphology and actin cytoskeletal polarization might produce important differences in the contractility in individual SFs. U2OS cells show high front-back polarization, which is reflected in strong enrichment of cofilin at the leading edge, where it promotes actin turnover and Arp2/3 debranching (Andrianantoandro and Pollard, 2006; Chan et al., 2000). Cofilin depletion would therefore likely impact the SF network most prominently at the leading edge, consistent with replacement of transverse arcs with immature geodesic structures in cofilin KD U2OS cells. HeLa cells are much less front-back polarized and show more uniform cofilin distribution and activity (Kim et al., 2009). Here, instead of actively nucleating or severing SFs at one end of the cell, cofilin may contribute to a radially symmetric cell shape by limiting contractility in any given SF. In the future, it would be valuable to explore this idea by systematically varying front-back polarization in a single cell type and investigating how cofilin depletion modulates SF mechanics.

Our study raises a number of open mechanistic questions. For example, while our results suggest that cofilin 'edits out' short actin filaments and branched actin filaments during arc maturation, we were unable to directly capture this process. High-speed superresolution imaging may lend new kinetic insights. Additionally, the mechanism through which cofilin is recruited to low-tension SFs remains unclear. As described above, reconstitution studies involving actin filaments and crosslinkers suggest that the conformation of actin might regulate cofilin binding and severing. Specifically, cofilin binding to F-actin is cooperative, with increased tension proposed to untwist the helical structure of actin, thereby preventing cofilin binding (Hayakawa et al., 2011). Furthermore, cofilin is reported to compete with tropomyosins, which might recruit NMMII, for actin-binding sites (Blanchoin et al., 2000; Chan et al., 2009; DesMarais et al., 2002; Hsiao et al., 2015; Jansen and Goode, 2019). This competition potentially serves as a mechanism for regulating cofilin binding and severing of SFs. However, others have suggested that filament torsion does not directly impact cofilin binding, which is not well understood and may be stochastic. Instead, cofilin binding may enhance filament severing by increasing the local torque applied from cofilin binding (Wioland et al., 2019). It is unclear whether similar mechanisms govern the disassembly of SFs, given that SFs are physically stabilized by crosslinkers and may be anchored to focal adhesions and other SFs. However, observations in live cells suggest that tension influences SF disassembly (Hayakawa et al., 2011; Tojkander et al., 2015). Experiments in which SFs are isolated from cells (e.g. via 'deroofing') and manipulated in the presence of cofilin may lend insight into the relative importance of applied tension and torsion in SF disassembly. Finally, while our findings suggest that cofilin is critical in regulating SF dynamics and cell and mechanical polarity, it is also implicated in a number of other cellular processes including transcription, G-actin transport and apoptosis (DesMarais et al., 2005; Kanellos and Frame, 2016). Thus, depletion of cofilin almost certainly influences other phenomena in this system besides mechanical polarity, which in turn underscores the value of obtaining direct and rapid mechanical measurements of single SFs. In the future, it will be interesting and important to determine whether cofilin contributes similarly to tension polarization in more tissue-mimetic matrix geometries, featuring more complex topography, mechanics and composition.

MATERIALS AND METHODS

Cell culture and transfection

U2OS cells (ATCC Cat# HBT-96, CVCL_0042) were cultured in Dulbecco's modified Eagle's medium (DMEM; Gibco) supplemented with 10% fetal bovine serum (FBS; JR Scientific), 1% non-essential amino acids (Gibco) and 1% penicillin/streptomycin (Gibco). Cells were transfected with Viafect Transfection Reagent (Promega) according to the manufacturer's protocol. Cells were tested for mycoplasma every three months and authenticated via short tandem repeat profiling.

Cloning and cell line generation

We used shRNA constructs targeting the cofilin-1 isoform (shCofilin_1: 5′-ACGACATGAGGTGCGTAAGT-3′, shCofilin_2: 5′-CCAGATAAGGA-CTGCCGCTAT-3′, shCofilin_3: 5′-AAGGAGGATCTGGTGTTTATC-3′). A non-targeting sequence (NT: 5′-GCTTCTAGCCAGTTACGTACA-3′) was also included as a control. Each oligonucleotide was inserted into the pLKO.1-TRC cloning vector (Addgene #10878) using AgeI and EcoRI (Moffat et al., 2006) and verified by sequencing. RFP–LifeAct was cloned into the pFUG vector as described previously (Lee et al., 2016).

Lentiviral particles were packaged in HEK 293T cells (provided by the David Schaffer laboratory at UC Berkeley, originally sourced from ATCC Cat# CRL-11268, CVCL_1926). shRNA viral particles were used to transduce U2OS cells at a multiplicity of infection (MOI) of 1. Cells were selected using 2 µg/ml puromycin (Clontech). Following confirmation of KD via western blotting and immunofluorescence characterization, cells were subsequently transduced with pFUG-RFP LifeAct (MOI 3).

Journal of Cell Science (2020) 133, jcs243873. doi:10.1242/jcs.243873

Constitutively active cofilin (EGFP–Cofilin_S3A), dominant negative cofilin (EGFP–Cofilin_S3D), and WT cofilin (EGFP–Cofilin_WT) plasmids were created by Hans Mannherz (Mannherz et al., 2005) and were shared by Klemens Rottner (Technische Universität Braunschweig, Germany). EGFP–Arp3 plasmid was Addgene #8462 (deposited by Matthew Welch; Welch et al., 1997).

Western blotting

Cells were lysed in RIPA buffer (Sigma) with phosphatase and protease inhibitors (EMD Millipore) and heated to 70°C. Samples were run on a 4–12% Bis-Tris gel (Thermo Fisher Scientific) and transferred to a PVDF membrane (Thermo Fisher Scientific). The following primary antibodies were used: rabbit anti-cofilin (1:1000; AB_11220230), rabbit anti-phosphorylated cofilin (1:1000; AB_2080597), mouse anti-GAPDH (1:5000, AB_1078992), mouse anti-β-actin (1:1000, AB_476697), and rabbit anti-ADF (1:1000, AB_476912). The following secondary antibodies were used: goat anti-mouse HRP-conjugate (1:5000; AB_2533947), goat anti-rabbit HRP-conjugate (3:5000; AB_2533967). HRP-conjugated bands were imaged using enhanced chemiluminescence reagent (ECL, Thermo Fisher Scientific).

F-actin:G-actin ratio quantification

The F- and G-actin ratio was quantified via differential Triton X-100 solubility and western blotting using a modified protocol described previously (Parreno et al., 2014). Cells were washed with PBS and scraped off polystyrene dishes. The cell suspension was centrifuged at 100 ***g*** for 3 min to pellet cells. The cell pellet was resuspended in an F-actin stabilization buffer [150 mM KCl, 20 mM HEPES, 2 mM $MgCl_2$, K_2HPO_4, 0.5% NP-40 (Fluka), pH 7.4] supplemented with 1× HALT protease inhibitor (Life Technologies) and agitated for 5 min. The suspension was then centrifuged at 15,000 ***g*** for 10 min at 4°C. The G-actin-containing supernatant was collected and the F-actin-containing pellet was resuspended in RIPA buffer. Both fractions were incubated on ice for 30 min with slight agitation. Equal volumes of each of the fractions were analyzed via western blotting as described above.

Immunostaining

Cells were rinsed briefly with DPBS and then fixed in 4% (v/v) paraformaldehyde (Alfa-Aeser) for 10 min at room temperature. Cells were permeabilized for 10 min in 0.3% (v/v) Triton X-100 (EMD Millipore) diluted in PBS containing 5% (v/v) goat serum (Thermo Fisher) for 10 min. Cells were blocked in PBS containing 5% (v/v) goat serum for 16 h at 4°C. Coverslips were incubated with primary antibodies for 2 h at room temperature, rinsed with 1% (v/v) goat serum in PBS, and then incubated with secondary antibodies and phalloidin for 1 h at room temperature in the dark. Nuclei were stained with Hoechst 33342 (1:500, Thermo Fisher Scientific) or DAPI (1:500, Sigma). Cells were rinsed in PBS and mounted using Fluoromount-G (Southern Biotech).

The following primary antibodies were used for immunostaining: mouse anti-vinculin hVin-1 (1:200, AB_795706), rabbit anti-di-phosphorylated myosin light chain Thr18/Ser19 (1:200, AB_2147464), mouse anti-α-actinin-1 (1:200, AB_476737), rabbit anti-cofilin (1:200, AB_11220230), rabbit anti-cofilin (1:200, AB_297714), mouse anti-filamin (1:200, AB_2247189), mouse anti-tropomyosin, recognizing tropomyosin isoforms 1, 2, 3 and 6 (1:200, AB_261632), rabbit anti-ADF (1:200, AB_476912) and rabbit anti-GFP (1:400, AB_305564). Alexa Fluor 488-conjugated anti-rabbit-IgG (1:400, AB_143165), Alexa Fluor 647-conjugated anti-mouse-IgG (1:400, AB_2535804) secondary antibodies were used, as well as phalloidin–Alexa Fluor 546 (1:200, AB_2632953).

Micropatterning

Micropatterns were made as described previously (Carpi et al., 2011; Kassianidou et al., 2017; Lee et al., 2018; Théry et al., 2006b; Tseng et al., 2011). Briefly, plasma-treated coverslips were incubated with 10 µg/ml poly-L-lysine conjugated to polyethylene glycol (PLL-g-PEG; SuSoS) in 10 mM HEPES, pH 7.4 for 1 h at room temperature. The coverslips were rinsed briefly with PBS and deionized water. Coverslips were placed on a quartz-chrome photomask bearing the micropattern features (Front Range Photomask), which were designed using AutoCAD (Autodesk). The assembly was then illuminated under 180 nm UV light (Jelight) for 15 min. Coverslips were rinsed briefly with PBS.

Imaging

Unpatterned or micropatterned coverslips were coated with 20 µg/ml fibronectin (EMD Millipore) in 100 mM bicarbonate solution, pH 8.5, overnight at 4°C and rinsed extensively. U2OS cells were seeded at 3000–5000 cells/cm^2 and allowed to adhere for 4–6 h before imaging or fixation. Prior to live-cell imaging, the medium was changed to Phenol Red-free DMEM (Gibco) supplemented with 10% FBS, 1% nonessential amino acids, 1% penicillin/streptomycin and 25 mM HEPES (imaging medium).

Confocal imaging

For laser ablation and fixed cell studies, an upright Olympus BX51WI microscope (Olympus Corporation) equipped with Swept Field Confocal Technology (Bruker) and a Ti:Sapphire 2-photon Chameleon Ultra II laser (Coherent) was used. The two-photon laser was set to 770 nm and single SF ablation was performed using three 20 ms pulses. Cells were imaged again at least 20 min after ablation to verify viability and membrane integrity. Live-cell imaging was performed using an Olympus LUMPlanFL N 60×/1.0 water dipping objective. Cells were kept at 37°C using a stage-top sample heater (Warner Instruments). Fixed cell imaging was performed using an Olympus UPlanSApo 60×/1.35 oil immersion objective at room temperature. Images were captured using an EM-CCD camera (Photometrics QuantEM:512SC). The following emission filters were used: Quad FF-01-446/523/600/677-25 (Semrock) and 525/50 ET525/50 (Chroma). PrairieView Software (v. 5.3 U3, Bruker) was used to acquire images.

Epifluorescence imaging

For fixed cell imaging studies, a Nikon Ti-E inverted microscope was used with a 60×/1.40 Plan Apo VC objective and a xenon arc lamp (Lambda LS, Sutter Instrument). For live-cell migration studies, a Nikon TE-2000 inverted microscope was used with a 10×/0.30 Ph1 DLL objective. The microscopes are equipped with a motorized programmable stage (Applied Scientific Instrumentation) and a stage-top sample heater to maintain optimal humidity, CO_2 levels, and temperature (In Vivo Scientific). Images were acquired with a cooled CCD Hamamatsu Orca-R2 (Ti-E microscope) or CoolSNAP HQ2 camera (TE-2000 microscope) and Nikon Elements 5.02.00 Software.

Structured illumination microscopy

Samples were fixed, stained, and mounted as described above. Samples were imaged using a Zeiss Elyra PS.1 structured illumination microscope (SIM) and a Plan-Apochromat 63x/1.4 oil DIC M27 objective (Zeiss). Zen 2010 software was used for image acquisition.

Traction force microscopy

Traction force microscopy experiments were performed as described previously (Plotnikov et al., 2014). Coverslips were cleaned briefly with 70% ethanol and plasma treated for 5 min before being incubated with a silanization solution consisting of 5% acetic acid and 0.3% bind-silane in 100% ethanol. Polyacrylamide gels were synthesized with 5% acrylamide (Bio-Rad), 0.2% bis-acrylamide (Bio-Rad), 1% ammonium persulfate (Bio-Rad), 0.1% tetramethylethylenediamine (TEMED, Bio-Rad) and 1.5% 0.2 µm-diameter dark red fluorescent microspheres (Thermo Fisher Scientific). 0.0001% 2-pyridinecarboxaldehyde was added to the precursor solution just prior to gel polymerization for subsequent fibronectin conjugation (Lee et al., 2016). A drop of the acrylamide precursor solution was polymerized between a silanized coverslip and a glass surface treated with a hydrophobic solution (RainX). The final gel height is ∼75 µm. Following polymerization, the gels were carefully removed from the hydrophobic surface and rinsed extensively in PBS. Gels were then incubated with 20 µg/ml fibronectin (EMD Millipore) in 100 mM bicarbonate solution, pH 8.5, overnight at 37°C and rinsed extensively. U2OS RFP-Lifeact cells were seeded at 2500 cells/cm^2 and allowed to

adhere for 4–6 h before imaging. Prior to imaging, the medium was changed to Phenol Red-free imaging medium. Images of the fluorescent microspheres and the cells were acquired before and after treatment with a 2% (w/v) SDS solution to remove cells. We computed maps of cellular traction stresses from bead positions before and after cell detachment using Fourier transform traction cytometry implemented using a modified ImageJ plugin (Martiel et al., 2015). Total traction forces were measured by summing the traction forces over the cell area.

Image analysis

For visualization purposes, image contrast was adjusted using FIJI (Rueden et al., 2017; Schindelin et al., 2012). Kymographs were generated by drawing a 1-pixel line perpendicular to the flow of transverse arcs and taking a re-slice. Time-lapse movies were registered using the Stack Reg plugin (Thevenaz et al., 1998) and corrected for photobleaching using the BleachCorr function. *Z*-stack images were reconstructed using the 3D Project function.

Stress fiber retraction

For SF ablation studies, images were acquired every 1.24 s for 77 s. The *xy*-coordinates of the two severed ends of the SF were manually tracked in ImageJ. The coordinates were used to calculate the half-distance between the severed ends, giving the retraction of one of the severed ends. The half-distance versus time curve was fitted to the following equation (Eqn 1) using the curvefit function in MATLAB:

$$L(t) = L_0\left(1 - \exp\left(-\frac{t}{\tau}\right)\right) + D_a, \quad (1)$$

where L_0 is the stored elastic energy of prestress of the fiber, τ is the viscoelastic time constant, and D_a is the fitted length of the fiber destroyed during ablation (Kumar et al., 2006).

Transverse arc prestress was measured by subtracting the distance between the severed ends at 45 s and the distance between the SF ends at 0 s and dividing by 2.

Cell height analysis

Z-stack images with 0.5 µm-spacing were acquired and reconstructed in ImageJ. Heights were manually measured from the base of the cell to the highest point.

Polarization analysis

Unpatterned cells were classified as polarized if the cell had a single lamella containing transverse arcs and dorsal SFs. Rounded cells with transverse arcs and dorsal SFs ringing the cell were classified as unpolarized. Cells on crossbows were classified as polarized if dorsal SFs and transverse arcs were present along the curved arc of the pattern.

Migration analysis

Phase-contrast images of cells were acquired every 10 min for at least 6 h. The centroid of the cell was tracked using the Manual Tracking plugin in ImageJ to obtain the frame-to-frame instantaneous speed. The instantaneous speeds were averaged over a 6 h window to obtain the average migration speed of the cell.

Statistical analysis

Statistical analyses and graph generation were performed using GraphPad Prism (v. 8.1.2). Samples were determined to be non-normal through the Shapiro–Wilk normality test. Non-parametric Kruskal–Wallis tests, followed by a post-hoc Dunn's test for multiple comparisons, were used to assess statistical differences in continuous data sets. In box plots, the top, middle, and bottom of the box represent the 75th, 50th (median) and 25th percentiles, respectively. The average is represented by the red cross. Bars extend to the maximum and minimum value of the data set. ANOVA followed by the Holm–Sidak test for multiple comparisons was used to compare average protein expression levels in western blots. The χ squared test was used to assess differences in the distributions of polarized versus non-polarized cells. Minimum sample sizes were calculated using a power of 0.8.

Acknowledgements

Laser ablation and confocal images were obtained at the CIRM/QB3 Shared Stem Cell Facility. Micropatterns were fabricated at the QB3 Biomolecular Nanotechnology Center. Structured Illumination Microscopy was performed at the UC Berkeley Biological Imaging Facility, which was supported in part by the NIH S10 program under award number 1S10(D018136-01). Western blots were imaged using equipment shared by the David Schaffer lab. We thank Mary West, Paul Lum, and Denise Schichnes for training and/or assistance. We also thank Carmen Chan and Badriprasad Ananthanarayanan for helpful discussion.

Competing interests

The authors declare no competing or financial interests.

Author contributions

Conceptualization: S.L., S.K.; Methodology: S.L., S.K.; Validation: S.L.; Formal analysis: S.L.; Investigation: S.L.; Resources: S.L., S.K.; Data curation: S.L.; Writing - original draft: S.L., S.K.; Writing - review & editing: S.L., S.K.; Visualization: S.L.; Supervision: S.K.; Project administration: S.K.; Funding acquisition: S.L., S.K.

Funding

Research reported in this publication was supported by the National Institutes of Health (NIH) [F31GM119329 to S.L., R01GM122375 to S.K. and R21EB016359 to S.K.] and the Siebel Scholars Program [to S.L.]. The content is solely the responsibility of the authors and does not necessarily represent the official views of the funding agencies. Deposited in PMC for release after 12 months.

Supplementary information

Supplementary information available online at
http://jcs.biologists.org/lookup/doi/10.1242/jcs.243873.supplemental

Peer review history

The peer review history is available online at
https://jcs.biologists.org/lookup/doi/10.1242/jcs.243873.reviewer-comments.pdf

References

Andrianantoandro, E. and Pollard, T. D. (2006). Mechanism of actin filament turnover by severing and nucleation at different concentrations of ADF/Cofilin. *Mol. Cell* **24**, 13-23. doi:10.1016/j.molcel.2006.08.006

Blanchoin, L., Pollard, T. D. and Mullins, R. D. (2000). Interactions of ADF/cofilin, Arp2/3 complex, capping protein and profilin in remodeling of branched actin filament networks. *Curr. Biol.* **10**, 1273-1282. doi:10.1016/S0960-9822(00)00749-1

Blanchoin, L., Boujemaa-Paterski, R., Sykes, C. and Plastino, J. (2014). Actin dynamics, architecture, and mechanics in cell motility. *Physiol. Rev.* **94**, 235-263. doi:10.1152/physrev.00018.2013

Bravo-Cordero, J. J., Magalhaes, M. A. O., Eddy, R. J., Hodgson, L. and Condeelis, J. (2013). Functions of cofilin in cell locomotion and invasion. *Nat. Rev. Mol. Cell Biol.* **14**, 405-415. doi:10.1038/nrm3609

Burnette, D. T., Shao, L., Ott, C., Pasapera, A. M., Fischer, R. S., Baird, M. A., Der Loughian, C., Delanoe-Ayari, H., Paszek, M. J., Davidson, M. W. et al. (2014). A contractile and counterbalancing adhesion system controls the 3D shape of crawling cells. *J. Cell Biol.* **205**, 83-96. doi:10.1083/jcb.201311104

Carpi, N., Piel, M., Azioune, A. and Fink, J. (2011). Micropatterning on glass with deep UV. *Protoc. Exch.* doi:10.1038/protex.2011.238

Chan, A. Y., Bailly, M., Zebda, N., Segall, J. E. and Condeelis, J. S. (2000). Role of cofilin in epidermal growth factor-stimulated actin polymerization and lamellipod protrusion. *J. Cell Biol.* **148**, 531-542. doi:10.1083/jcb.148.3.531

Chan, C., Beltzner, C. C. and Pollard, T. D. (2009). Cofilin dissociates Arp2/3 complex and branches from actin filaments. *Curr. Biol.* **19**, 537-545. doi:10.1016/j.cub.2009.02.060

Chang, C.-W. and Kumar, S. (2013). Vinculin tension distributions of individual stress fibers within cell-matrix adhesions. *J. Cell Sci.* **126**, 3021-3030. doi:10.1242/jcs.119032

Chen, Q. and Pollard, T. D. (2011). Actin filament severing by cofilin is more important for assembly than constriction of the cytokinetic contractile ring. *J. Cell Biol.* **195**, 485-498. doi:10.1083/jcb.201103067

Cramer, L. P., Siebert, M. and Mitchison, T. J. (1997). Identification of novel graded polarity actin filament bundles in locomoting heart fibroblasts: implications for the generation of motile force. *J. Cell Biol.* **136**, 1287-1305. doi:10.1083/jcb.136.6.1287

DesMarais, V., Ichetivkin, I., Condeelis, J. and Hitchcock-DeGregori, S. E. (2002). Spatial regulation of actin dynamics: a tropomyosin-free, actin-rich compartment at the leading edge. *J. Cell Sci.* **115**, 4649-4660. doi:10.1242/jcs.00147

DesMarais, V., Macaluso, F., Condeelis, J. and Bailly, M. (2004). Synergistic interaction between the Arp2/3 complex and cofilin drives stimulated lamellipod extension. *J. Cell Sci.* **117**, 3499-3510. doi:10.1242/jcs.01211

DesMarais, V., Ghosh, M., Eddy, R. and Condeelis, J. (2005). Cofilin takes the lead. *J. Cell Sci.* **118**, 19-26. doi:10.1242/jcs.01631

Friedl, P. and Gilmour, D. (2009). Collective cell migration in morphogenesis, regeneration and cancer. *Nat. Rev. Mol. Cell Biol.* **10**, 445-457. doi:10.1038/nrm2720
Hayakawa, K., Tatsumi, H. and Sokabe, M. (2011). Actin filaments function as a tension sensor by tension-dependent binding of cofilin to the filament. *J. Cell Biol.* **195**, 721-727. doi:10.1083/jcb.201102039
Ho, C. Y. and Lammerding, J. (2012). Lamins at a glance. *J. Cell Sci.* **125**, 2087-2093. doi:10.1242/jcs.087288
Hotulainen, P. and Lappalainen, P. (2006). Stress fibers are generated by two distinct actin assembly mechanisms in motile cells. *J. Cell Biol.* **173**, 383-394. doi:10.1083/jcb.200511093
Hotulainen, P., Paunola, E., Vartiainen, M. K. and Lappalainen, P. (2005). Actin-depolymerizing factor and Cofilin-1 play overlapping roles in promoting rapid F-actin depolymerization in mammalian nonmuscle cells. *Mol. Biol. Cell* **16**, 649-664. doi:10.1091/mbc.e04-07-0555
Hsiao, J. Y., Goins, L. M., Petek, N. A. and Mullins, R. D. (2015). Arp2/3 complex and cofilin modulate binding of tropomyosin to branched actin networks. *Curr. Biol.* **25**, 1573-1582. doi:10.1016/j.cub.2015.04.038
Huttenlocher, A. and Horwitz, A. R. (2011). Integrins in cell migration. *Cold Spring Harb. Perspect. Biol.* **3**, a005074. doi:10.1101/cshperspect.a005074
Jansen, S. and Goode, B. L. (2019). Tropomyosin isoforms differentially tune actin filament length and disassembly. *Mol. Biol. Cell* **30**, 671-679. doi:10.1091/mbc.E18-12-0815
Kanellos, G. and Frame, M. C. (2016). Cellular functions of the ADF/cofilin family at a glance. *J. Cell Sci.* **129**, 3211-3218. doi:10.1242/jcs.187849
Kanellos, G., Zhou, J., Patel, H., Ridgway, R. A., Huels, D., Gurniak, C. B., Sandilands, E., Carragher, N. O., Sansom, O. J., Witke, W. et al. (2015). ADF and Cofilin1 control actin stress fibers, nuclear integrity, and cell survival. *Cell Rep.* **13**, 1949-1964. doi:10.1016/j.celrep.2015.10.056
Kassianidou, E., Brand, C. A., Schwarz, U. S. and Kumar, S. (2017). Geometry and network connectivity govern the mechanics of stress fibers. *Proc. Natl. Acad. Sci. USA* **114**, 2622-2627. doi:10.1073/pnas.1606649114
Kim, J.-S., Huang, T. Y. and Bokoch, G. M. (2009). Reactive oxygen species regulate a slingshot-cofilin activation pathway. *Mol. Biol. Cell* **20**, 2650-2660. doi:10.1091/mbc.e09-02-0131
Kumar, S., Maxwell, I. Z., Heisterkamp, A., Polte, T. R., Lele, T. P., Salanga, M., Mazur, E. and Ingber, D. E. (2006). Viscoelastic retraction of single living stress fibers and its impact on cell shape, cytoskeletal organization, and extracellular matrix mechanics. *Biophys. J.* **90**, 3762-3773. doi:10.1529/biophysj.105.071506
Kumar, A., Shutova, M. S., Tanaka, K., Iwamoto, D. V., Calderwood, D. A., Svitkina, T. M. and Schwartz, M. A. (2019). Filamin A mediates isotropic distribution of applied force across the actin network. *J. Cell Biol.* **218**, 2481-2491. doi:10.1083/jcb.201901086
Lai, F. P. L., Szczodrak, M., Block, J., Faix, J., Breitsprecher, D., Mannherz, H. G., Stradal, T. E. B., Dunn, G. A., Small, J. V. and Rottner, K. (2008). Arp2/3 complex interactions and actin network turnover in lamellipodia. *EMBO J.* **27**, 982-992. doi:10.1038/emboj.2008.34
Lazarides, E. (1976). Actin, alpha-actinin, and tropomyosin interaction in the structural organization of actin filaments in nonmuscle cells. *J. Cell Biol.* **68**, 202-219. doi:10.1083/jcb.68.2.202
Lee, S. and Kumar, S. (2016). Actomyosin stress fiber mechanosensing in 2D and 3D. *F1000Research* **5**, 2261. doi:10.12688/f1000research.8800.1
Lee, J. P., Kassianidou, E., MacDonald, J. I., Francis, M. B. and Kumar, S. (2016). N-terminal specific conjugation of extracellular matrix proteins to 2-pyridinecarboxaldehyde functionalized polyacrylamide hydrogels. *Biomaterials* **102**, 268-276. doi:10.1016/j.biomaterials.2016.06.022
Lee, S., Kassianidou, E. and Kumar, S. (2018). Actomyosin stress fiber subtypes have unique viscoelastic properties and roles in tension generation. *Mol. Biol. Cell* **29**, 1992-2004. doi:10.1091/mbc.E18-02-0106
Livne, A. and Geiger, B. (2016). The inner workings of stress fibers—from contractile machinery to focal adhesions and back. *J. Cell Sci.* **129**, 1293-1304. doi:10.1242/jcs.180927
Luo, W., Yu, C.-H., Lieu, Z. Z., Allard, J., Mogilner, A., Sheetz, M. P. and Bershadsky, A. D. (2013). Analysis of the local organization and dynamics of cellular actin networks. *J. Cell Biol.* **202**, 1057-1073. doi:10.1083/jcb.201210123
Luo, W., Lieu, Z. Z., Manser, E., Bershadsky, A. D. and Sheetz, M. P. (2016). Formin DAAM1 organizes actin filaments in the cytoplasmic nodal actin network. *PLoS ONE* **11**, e0163915. doi:10.1371/journal.pone.0163915
Mannherz, H. G., Gonsior, S. M., Gremm, D., Wu, X., Pope, B. J. and Weeds, A. G. (2005). Activated cofilin colocalises with Arp2/3 complex in apoptotic blebs during programmed cell death. *Eur. J. Cell Biol.* **84**, 503-515. doi:10.1016/j.ejcb.2004.11.008
Martiel, J.-L., Leal, A., Kurzawa, L., Balland, M., Wang, I., Vignaud, T., Tseng, Q. and Théry, M. (2015). Measurement of cell traction forces with ImageJ. *Methods Cell Biol.* **125**, 269-287. doi:10.1016/bs.mcb.2014.10.008
Moffat, J., Grueneberg, D. A., Yang, X., Kim, S. Y., Kloepfer, A. M., Hinkle, G., Piqani, B., Eisenhaure, T. M., Luo, B., Grenier, J. K. et al. (2006). A lentiviral RNAi library for human and mouse genes applied to an arrayed viral high-content screen. *Cell* **124**, 1283-1298. doi:10.1016/j.cell.2006.01.040
Nakamura, F., Stossel, T. P. and Hartwig, J. H. (2011). The filamins. *Cell Adh. Migr.* **5**, 160-169. doi:10.4161/cam.5.2.14401
Ono, S. and Ono, K. (2002). Tropomyosin inhibits ADF/cofilin-dependent actin filament dynamics. *J. Cell Biol.* **156**, 1065-1076. doi:10.1083/jcb.200110013
Osborn, M., Born, T., Koitsch, H.-J. and Weber, K. (1978). Stereo immunofluorescence microscopy: I. Threedimensional arrangement of microfilaments, microtubules and tonofilaments. *Cell* **14**, 477-488. doi:10.1016/0092-8674(78)90234-9
Parreno, J., Raju, S., Niaki, M. N., Andrejevic, K., Jiang, A., Delve, E. and Kandel, R. (2014). Expression of type I collagen and tenascin C is regulated by actin polymerization through MRTF in dedifferentiated chondrocytes. *FEBS Lett.* **588**, 3677-3684. doi:10.1016/j.febslet.2014.08.012
Parsons, J. T., Horwitz, A. R. and Schwartz, M. A. (2010). Cell adhesion: integrating cytoskeletal dynamics and cellular tension. *Nat. Rev. Mol. Cell Biol.* **11**, 633-643. doi:10.1038/nrm2957
Petrie, R. J. and Yamada, K. M. (2012). At the leading edge of three-dimensional cell migration. *J. Cell Sci.* **125**, 5917-5926. doi:10.1242/jcs.093732
Plotnikov, S. V., Sabass, B., Schwarz, U. S. and Waterman, C. M. (2014). High-resolution traction force microscopy. *Methods Cell Biol.* **123**, 367-394. doi:10.1016/B978-0-12-420138-5.00020-3
Ridley, A. J., Schwartz, M. A., Burridge, K., Firtel, R. A., Ginsberg, M. H., Borisy, G. G., Parsons, J. T. and Horwitz, A. R. (2003). Cell migration: integrating signals from front to back. *Science* **302**, 1704-1709. doi:10.1126/science.1092053
Rueden, C. T., Schindelin, J., Hiner, M. C., DeZonia, B. E., Walter, A. E., Arena, E. T. and Eliceiri, K. W. (2017). ImageJ2: ImageJ for the next generation of scientific image data. *BMC Bioinformatics* **18**, 529. doi:10.1186/s12859-017-1934-z
Schindelin, J., Arganda-Carreras, I., Frise, E., Kaynig, V., Longair, M., Pietzsch, T., Preibisch, S., Rueden, C., Saalfeld, S., Schmid, B. et al. (2012). Fiji: an open-source platform for biological-image analysis. *Nat. Methods* **9**, 676-682. doi:10.1038/nmeth.2019
Small, J. V., Rottner, K., Kaverina, I. and Anderson, K. I. (1998). Assembling an actin cytoskeleton for cell attachment and movement. *Biochim. Biophys. Acta Mol. Cell Res.* **1404**, 271-281. doi:10.1016/S0167-4889(98)00080-9
Tanner, K., Boudreau, A., Bissell, M. J. and Kumar, S. (2010). Dissecting regional variations in stress fiber mechanics in living cells with laser nanosurgery. *Biophys. J.* **99**, 2775-2783. doi:10.1016/j.bpj.2010.08.071
Tee, Y. H., Shemesh, T., Thiagarajan, V., Hariadi, R. F., Anderson, K. L., Page, C., Volkmann, N., Hanein, D., Sivaramakrishnan, S., Kozlov, M. M. et al. (2015). Cellular chirality arising from the self-organization of the actin cytoskeleton. *Nat. Cell Biol.* **17**, 445-457. doi:10.1038/ncb3137
Thery, M., Racine, V., Piel, M., Pepin, A., Dimitrov, A., Chen, Y., Sibarita, J.-B. and Bornens, M. (2006a). Anisotropy of cell adhesive microenvironment governs cell internal organization and orientation of polarity. *Proc. Natl. Acad. Sci. USA* **103**, 19771-19776. doi:10.1073/pnas.0609267103
Théry, M., Pépin, A., Dressaire, E., Chen, Y. and Bornens, M. (2006b). Cell distribution of stress fibres in response to the geometry of the adhesive environment. *Cell Motil. Cytoskelet.* **63**, 341-355. doi:10.1002/cm.20126
Thevenaz, P., Ruttimann, U. E. and Unser, M. (1998). A pyramid approach to subpixel registration based on intensity. *IEEE Trans. Image Process.* **7**, 27-41. doi:10.1109/83.650848
Tojkander, S., Gateva, G., Schevzov, G., Hotulainen, P., Naumanen, P., Martin, C., Gunning, P. W. and Lappalainen, P. (2011). A molecular pathway for myosin II recruitment to stress fibers. *Curr. Biol.* **21**, 539-550. doi:10.1016/j.cub.2011.03.007
Tojkander, S., Gateva, G., Husain, A., Krishnan, R. and Lappalainen, P. (2015). Generation of contractile actomyosin bundles depends on mechanosensitive actin filament assembly and disassembly. *eLife* **4**, e06126. doi:10.7554/eLife.06126
Tseng, Q., Wang, I., Duchemin-Pelletier, E., Azioune, A., Carpi, N., Gao, J., Filhol, O., Piel, M., Théry, M. and Balland, M. (2011). A new micropatterning method of soft substrates reveals that different tumorigenic signals can promote or reduce cell contraction levels. *Lab. Chip* **11**, 2231. doi:10.1039/c0lc00641f
Vicente-Manzanares, M., Webb, D. J. and Horwitz, A. R. (2005). Cell migration at a glance. *J. Cell Sci.* **118**, 4917-4919. doi:10.1242/jcs.02662
Welch, M. D., DePace, A. H., Verma, S., Iwamatsu, A. and Mitchison, T. J. (1997). The human Arp2/3 complex is composed of evolutionarily conserved subunits and is localized to cellular regions of dynamic actin filament assembly. *J. Cell Biol.* **138**, 375-384. doi:10.1083/jcb.138.2.375
Wiggan, O. N., Shaw, A. E., DeLuca, J. G. and Bamburg, J. R. (2012). ADF/cofilin regulates actomyosin assembly through competitive inhibition of myosin II binding to F-actin. *Dev. Cell* **22**, 530-543. doi:10.1016/j.devcel.2011.12.026
Wiggan, O. N., Schroder, B., Krapf, D., Bamburg, J. R. and DeLuca, J. G. (2017). Cofilin regulates nuclear architecture through a myosin-II dependent mechanotransduction module. *Sci. Rep.* **7**, 40953. doi:10.1038/srep40953
Wioland, H., Guichard, B., Senju, Y., Myram, S., Lappalainen, P., Jégou, A. and Romet-Lemonne, G. (2017). ADF/cofilin accelerates actin dynamics by severing filaments and promoting their depolymerization at both ends. *Curr. Biol.* **27**, 1956-1967.e7. doi:10.1016/j.cub.2017.05.048
Wioland, H., Jegou, A. and Romet-Lemonne, G. (2019). Torsional stress generated by ADF/cofilin on cross-linked actin filaments boosts their severing. *Proc. Natl. Acad. Sci. USA* **116**, 2595-2602. doi:10.1073/pnas.1812053116

Supplementary Figures

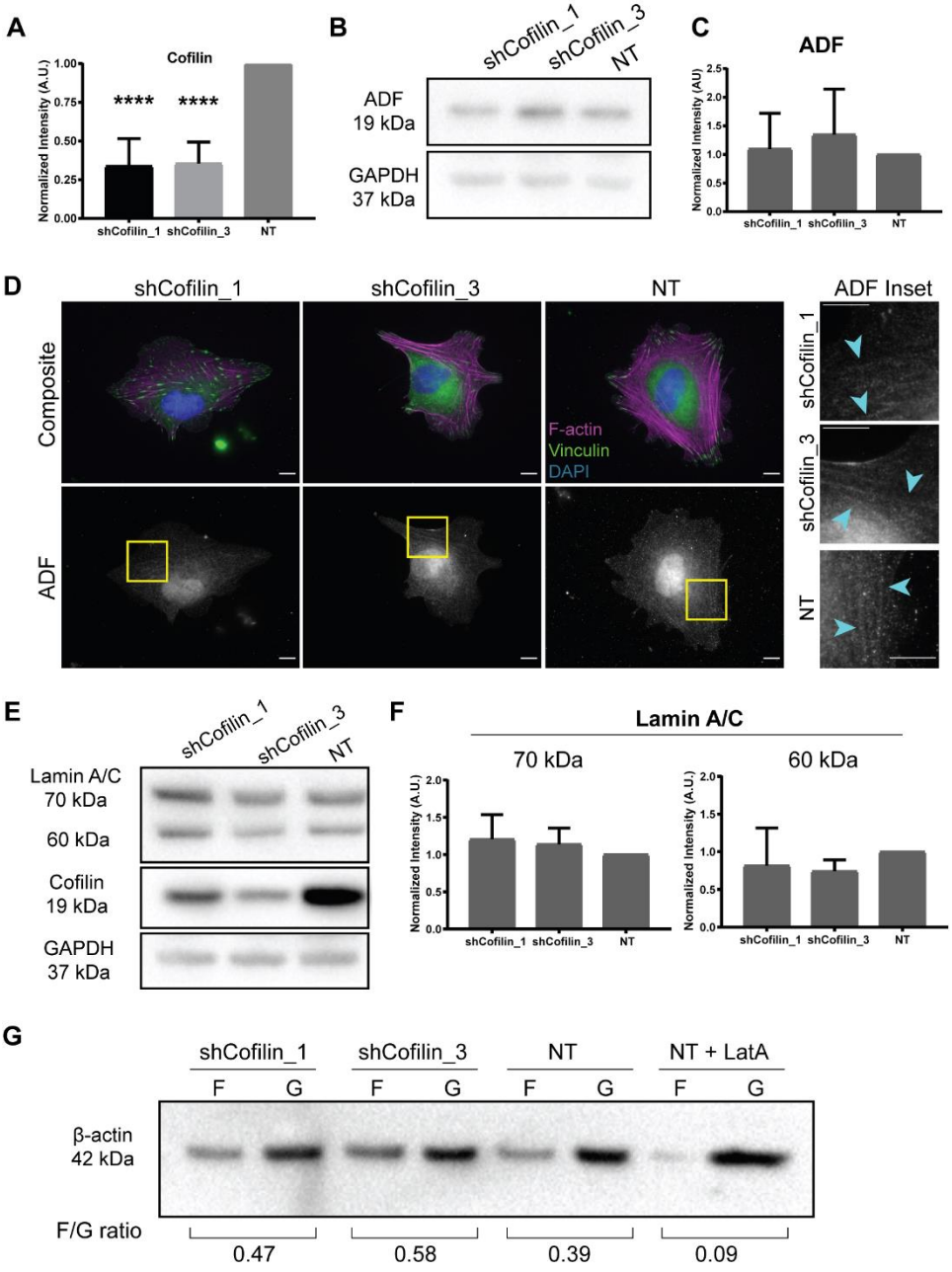

Figure S1. **Cofilin depletion does not affect ADF or lamin A/C expression levels.** (A) Average cofilin KD efficiency normalized to GAPDH loading controls. **** $p < 0.0001$, ANOVA, followed by post-hoc Holm-Sidak test. N = 7 independent experiments. (B) Western blot probing for ADF in cofilin-depleted cells. (C) Average ADF expression normalized to GAPDH loading control. N = 4 replicates across 2 independent experiments. (D) Cofilin KD or NT cells stained for F-actin (magenta), vinculin (green), nuclei (DAPI, blue), and ADF (gray). Right panel shows inset

indicated in ADF image. Blue arrows point to ADF localization to SFs. Scale bars: 10 µm. N = 20, 22, and 23 shCofilin_1, shCofilin_3, and NT cells across 1 experiment. (E) Western blots probing for Lamin A/C, cofilin, and loading control GAPDH. (F) Average expression of 70 and 60 kDa forms of Lamin A/C normalized to GAPDH loading control. N = 4 replicates across 2 independent experiments. (G) Western blots probing for ratio of F-actin and G-actin in cell lysates in cofilin KD, NT controls, and NT cells treated with 2 µM Latrunculin A to sequester actin in the G-actin form. Values indicate ratio of band intensities. Plots in (A), (C), and (F) show the average normalized integrated density, with error bars representing the standard deviation.

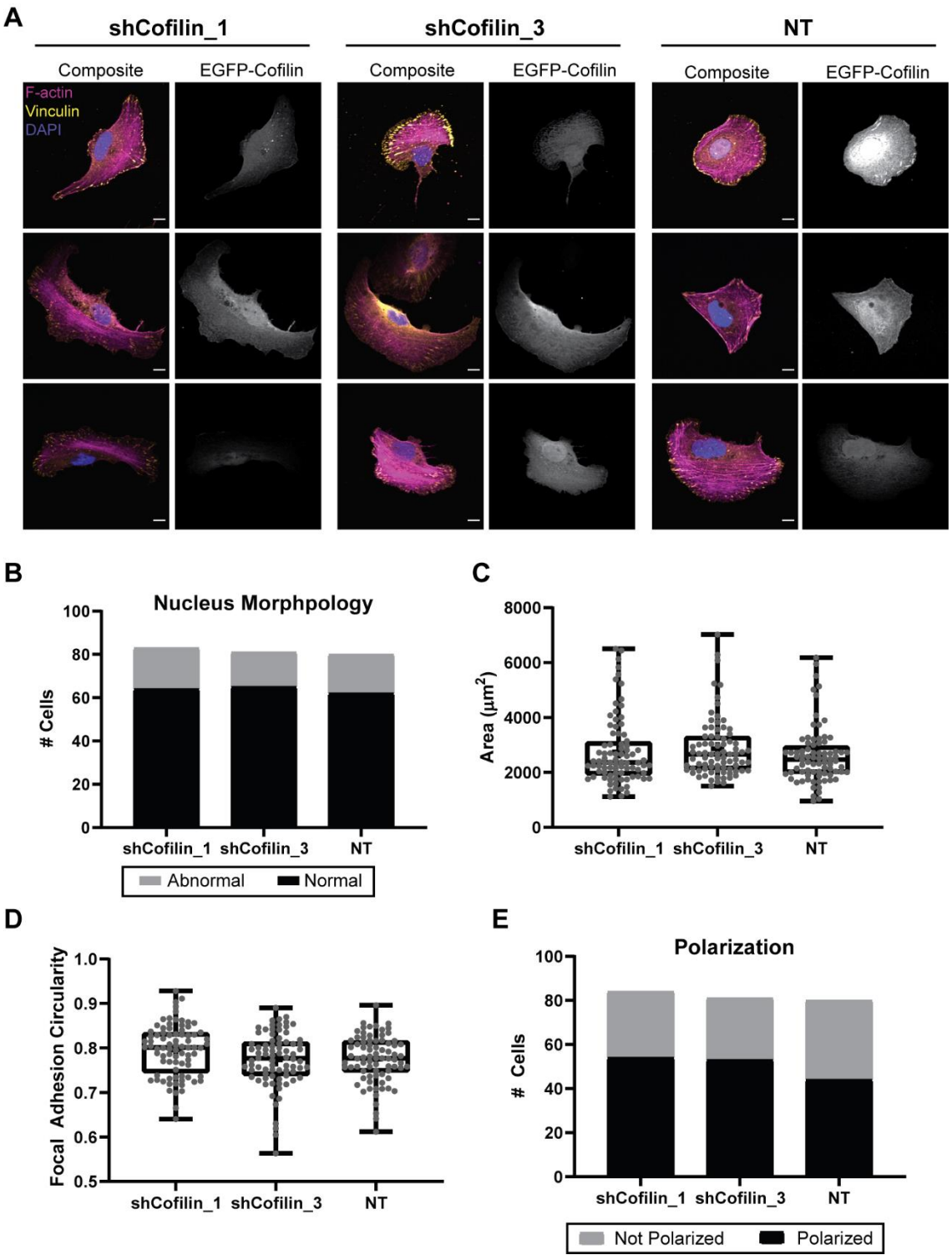

Figure S2. Transfection with cofilin-WT construct rescues phenotypic differences in cofilin KD cells. (A) Representative images of cofilin KD or NT cells transfected with EGFP-cofilin WT. Magenta: F-actin/phalloidin, yellow: vinculin, blue: DAPI, gray: EGFP-cofilin. Scale bar: 10 µm. (B) Distribution of transfected cells with abnormal or normal nuclei. (C) Distribution of cell spread

areas of transfected cells. (D) Distribution of focal adhesion circularity in cells expressing EGFP-cofilin. Each point represents the average focal adhesion circularity for one cell. (E) Distribution of cell polarities in cells expressing EGFP-cofilin. In all panels, distributions across conditions are not statistically significant. N = 84, 81, and 80, shCofilin_1, shCofilin_3, and NT cells, respectively, across 3 independent experiments. Boxes show the 25th, 50th, and 75th percentiles, with whiskers extending to the maximum and minimum. The cross indicates the mean.

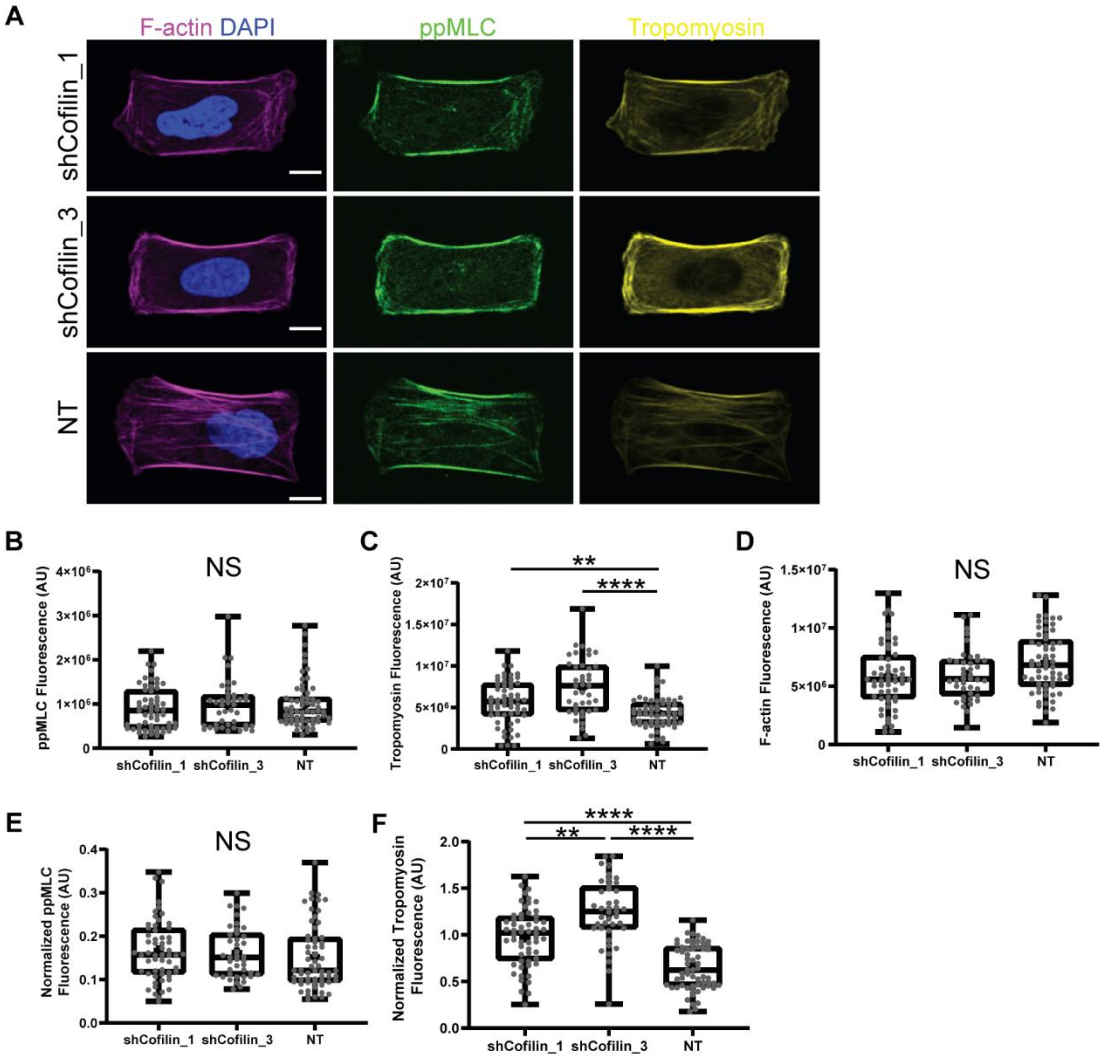

Figure S3. SFs in U-patterned cells contain more tropomyosin. (A) U-patterned cells fixed and stained for F-actin (magenta), DAPI (blue), ppMLC (green), and tropomyosin (yellow). Scale bar: 10 µm. Representative cells are shown from 2 independent experiments. (B) Distribution of integrated ppMLC fluorescence intensities along the top SF spanning the gap of the U-pattern. (C) Distribution of integrated tropomyosin fluorescence intensities along the top SF spanning the gap of the U-pattern. (D) Distribution of integrated F-actin fluorescence intensities along the top SF spanning the gap of the U-pattern. (E) Distribution of ppMLC fluorescence intensities normalized to F-actin fluorescent intensity. (F) Distribution of tropomyosin fluorescence intensities normalized to F-actin fluorescent intensity. ** $p < 0.01$, **** $p < 0.0001$, NS: not significant. Kruskal-Wallis test, post-hoc Dunn's test. N = 57. 41, and 61 stress fibers from different shCofilin_1, shCofilin_3, and NT cells, respectively, across 2 independent experiments. Boxes

show the 25th, 50th, and 75th percentiles, with whiskers extending to the maximum and minimum. The cross indicates the mean.

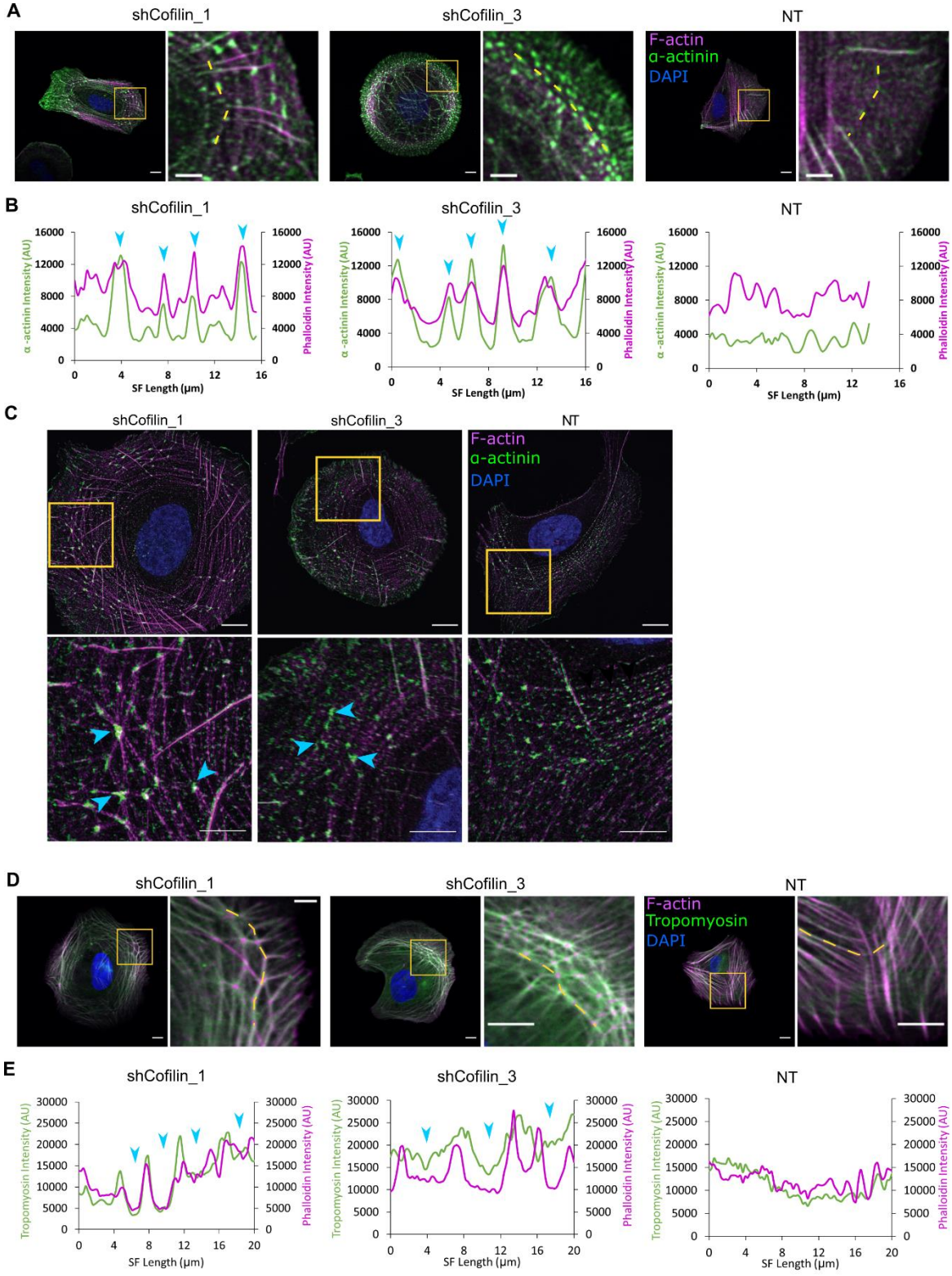

Figure S4. **Transverse arc nodes are enriched in α-actinin and devoid of tropomyosin.** (A) Confocal images of cofilin KD and NT cells stained for F-actin (magenta), α-actinin (green), and DAPI (blue). Images reproduced from Fig. 4C. (B) Linescans along transverse arcs (indicated by the dashed yellow line in panel A) in the α-actinin (green) and phalloidin (magenta) channels. Blue arrow heads indicate nodal regions of α-actinin clusters. (C) SIM images of cofilin KD and NT cells stained for F-actin (magenta), α-actinin (green), and DAPI (blue). Blue arrowheads point to α-actinin clusters at nodal points. White arrows point to small, periodic α-actinin clusters**.** (D) Confocal images of cofilin KD and NT cells stained for F-actin (magenta), tropomyosin (green), and DAPI (blue). Images reproduced from Fig. 4D. (E) Linescans along transverse arcs (indicated by the dashed yellow line in panel A) in the tropomyosin (green) and phalloidin (magenta) channels. Blue arrow heads indicate nodal regions devoid of tropomyosin. Scale bars for all panels: 10 µm, Inset: 5 µm.

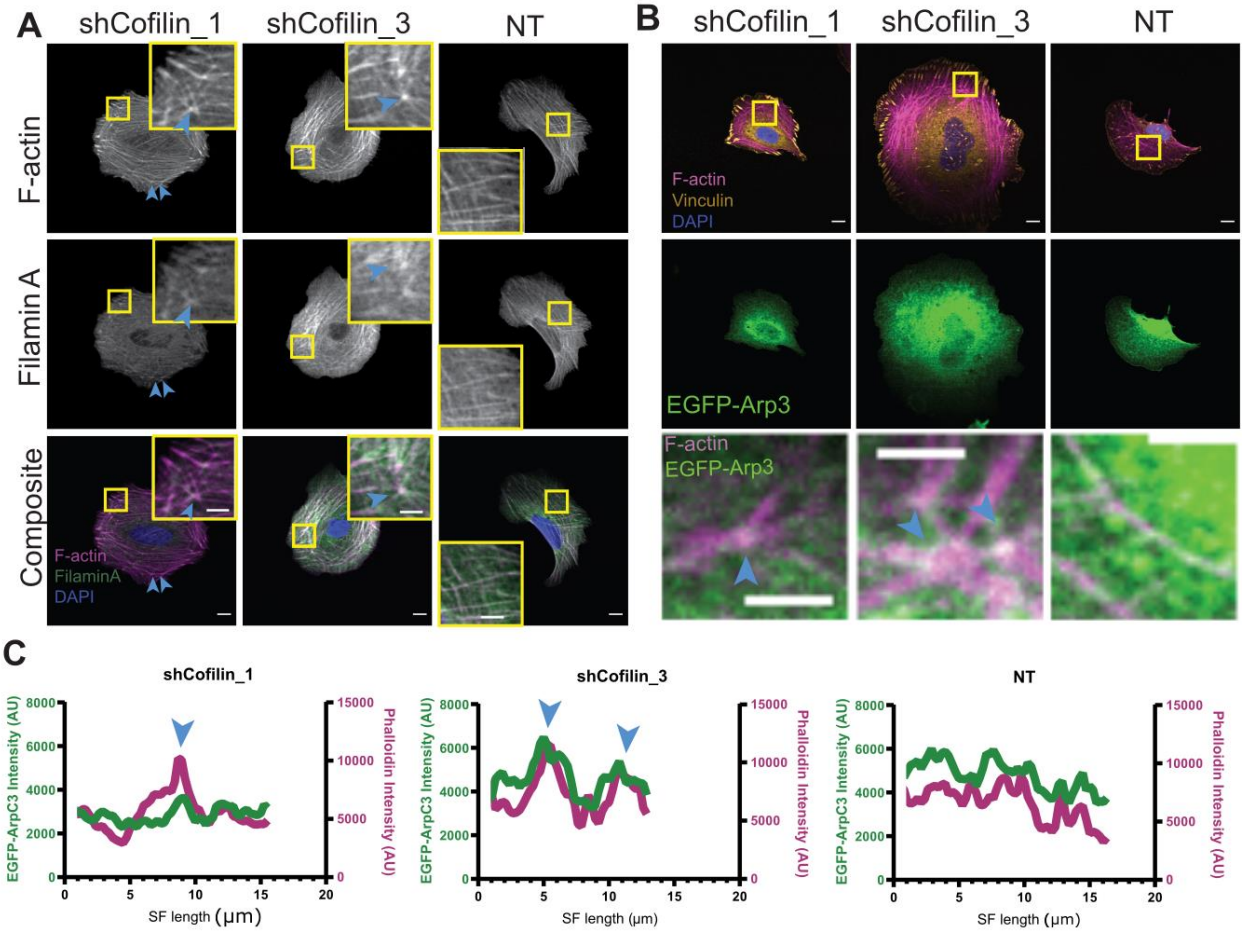

Figure S5. Transverse arc nodes are enriched in crosslinkers filamin A and Arp3. (A) Cells stained for F-actin (magenta), filamin A (green), and DAPI (blue). Blue arrowheads point to nodes. (B) Cells transfected with EGFP-Arp3 subunit (green) and stained for F-actin (magenta), vinculin (yellow), and nuclei (DAPI, blue). Blue arrowheads point to nodes. (E) Example linescans along transverse arcs for F-actin (magenta) and Arp3 (green). Blue arrowheads point to nodes. Scale bars for all panels: 10 μm, Inset: 5 μm. Representative images shown taken from samples sizes of N = 36, 39, and 37 shCofilin_1, shCofilin_3, and NT cells, respectively, across 2 independent experiments.

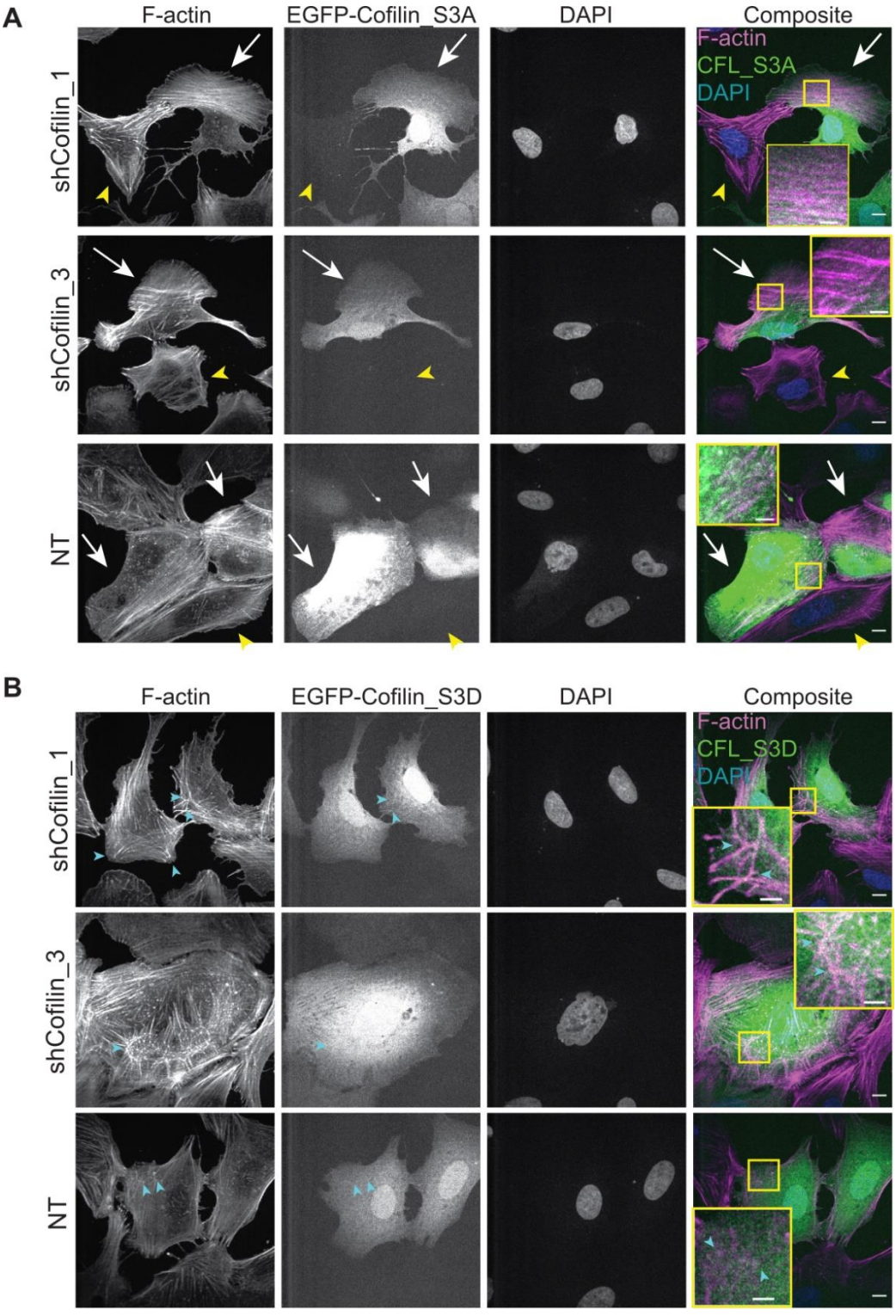

Figure S6. Cofilin KD cells regain a polarized SF phenotype when transfected with constitutively active cofilin. (A) shCofilin_1, shCofilin_3, and NT cells transfected with cofilin_S3A (constitutively active, non-phosphorlyatable), indicated by white arrows. Yellow

arrows indicate non-polarized cells not transfected with cofilin_S3A. Representative images shown from a sample size of 10 cells for each condition across 1 independent experiment. (B) shCofilin_1, shCofilin_3, and NT cells transfected with cofilin_S3D (dominant negative, phosphomimetic). Blue arrows point to multiple protrusions or nodes present in transfected cells. Cells are stained for F-actin (magenta) and DAPI (blue) and express an EGFP-fused cofilin mutant. Representative images shown from a sample size of 9, 10, and 10 shCofilin_1, shCofilin_3, and NT cells, respectively, across 1 independent experiment.

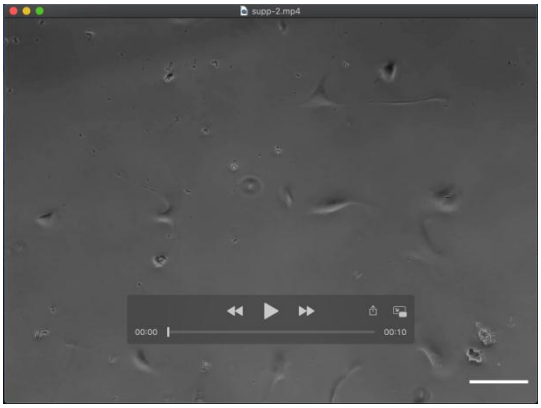

Movie 1. shCofilin_1 cells migrating on a surface uniformly-coated with fibronectin. Movie corresponds to Figure 1G. Colored lines indicate tracks used to determine migration speeds. Time: hh:mm:ss. Scale bar: 10 µm.

Movie 2. shCofilin_3 cells migrating on a surface uniformly-coated with fibronectin. Movie corresponds to Figure 1G. Colored lines indicate tracks used to determine migration speeds. Time: hh:mm:ss. Scale bar: 10 µm.

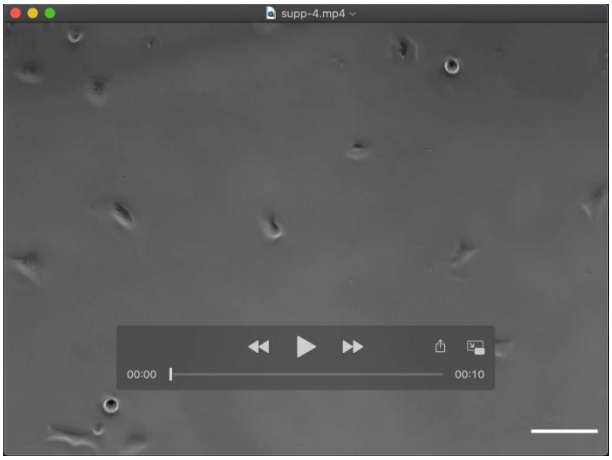

Movie 3. NT cells migrating on a surface uniformly-coated with fibronectin. Movie corresponds to Figure 1G. Colored lines indicate tracks used to determine migration speeds. Time: hh:mm:ss. Scale bar: 10 µm.

Movie 4. Ablation of single SF in patterned cofilin KD (left and middle panel) and NT cells. The SF on top of the fibronectin U-pattern is severed and its retraction is tracked over time. Movie corresponds to Figure 3A and B. SFs are visualized with Lifeact-RFP. Time: hh:mm:ss. Scale bar: 10 µm.

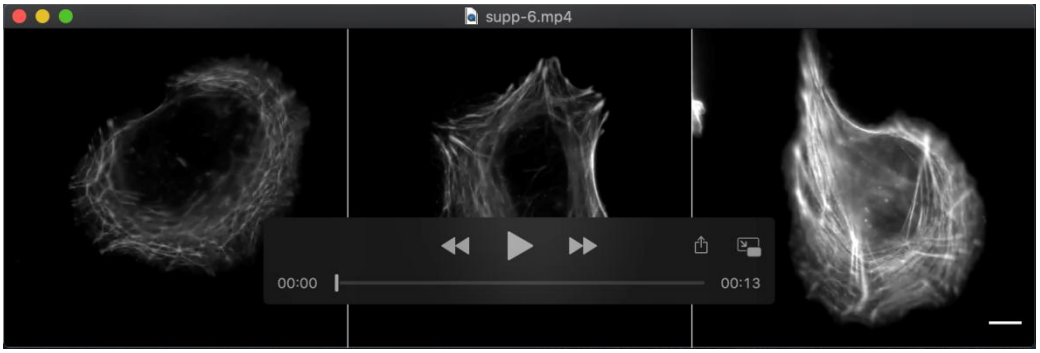

Movie 5. Stress fiber movement in cofilin KD and NT cells. Red arrows point to transverse arcs fusing together to form thicker SFs. Movie corresponds to Figure 4A. Cells are visualized with Lifeact-RFP. Time: hh:mm:ss. Scale bar: 10 µm.

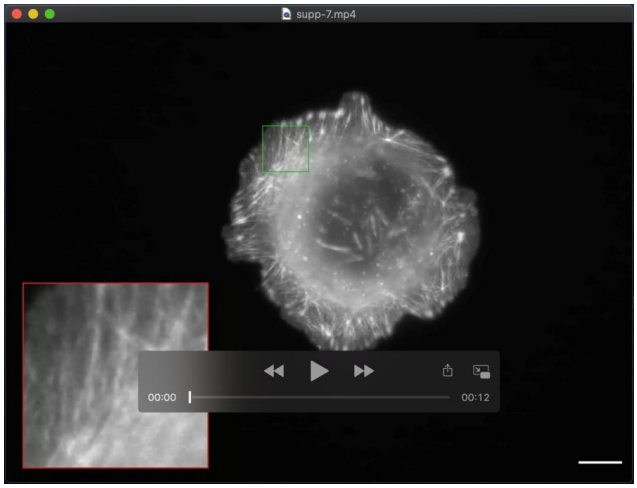

Movie 6. Node formation and movement in shCofilin_1 cell. Movie corresponds to Figure 4E. Cell is visualized with Lifeact-RFP. Time: hh:mm:ss. Scale bar: 10 µm.

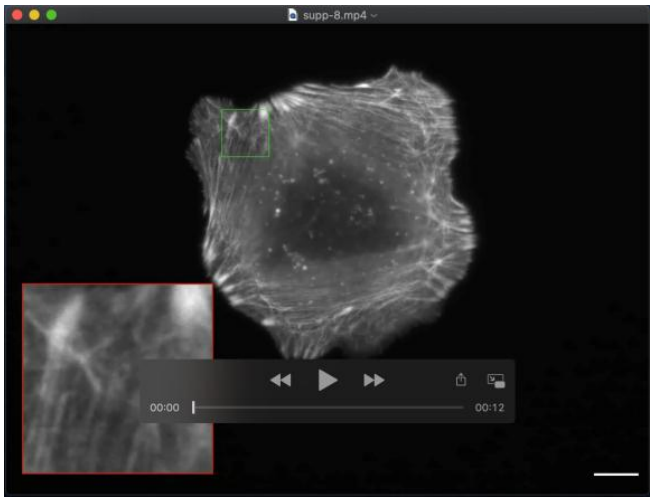

Movie 7. Node formation and movement in shCofilin_3 cell. Movie corresponds to Figure 4E. Cell is visualized with Lifeact-RFP. Time: hh:mm:ss. Scale bar: 10 µm.

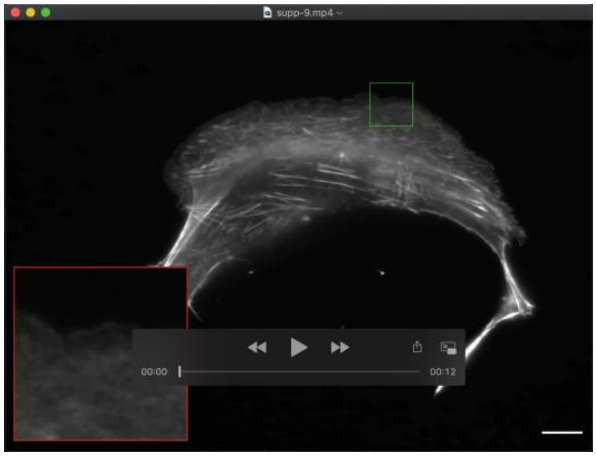

Movie 8. SF movement and transverse arc fusion in NT cell. Nodes do not form in this cell during the course of imaging. Movie corresponds to Figure 4E. Cell is visualized with Lifeact-RFP. Time: hh:mm:ss. Scale bar: 10 µm.

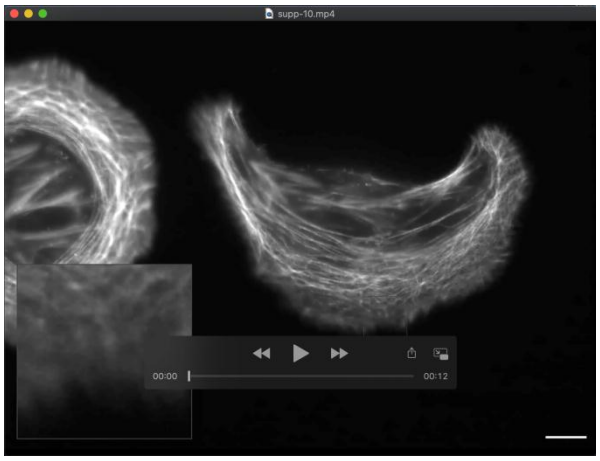

Movie 9. Node formation, movement, and resolution in NT cell. Transient nodes form and are resorbed into transverse arcs during retrograde stress fiber movement. Movie corresponds to Figure 4E. Cell is visualized with Lifeact-RFP. Time: hh:mm:ss. Scale bar: 10 µm.

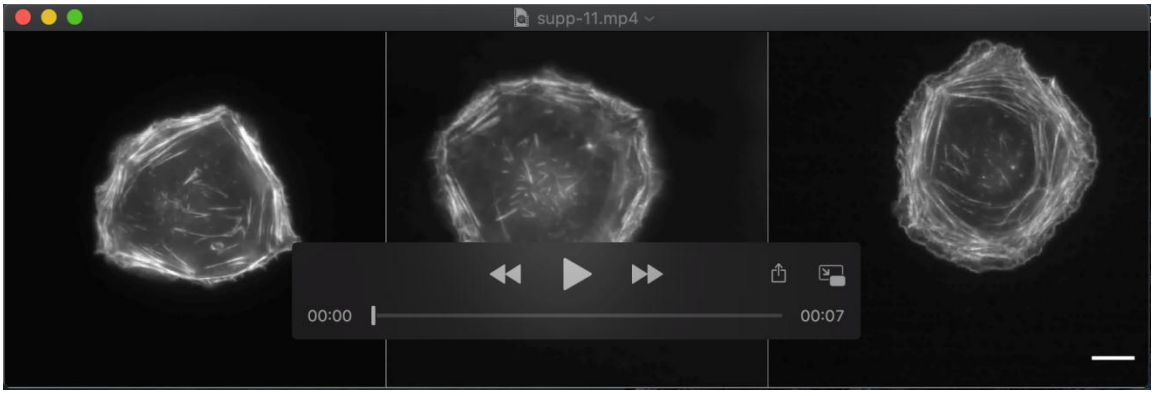

Movie 10. Timelapse images tracking cofilin KD and NT cells before and after EGF treatment to induce a polarized phenotype. Movie corresponds to Figure 6C. Cells are visualized with Lifeact-RFP. Time: hh:mm:ss from addition of 100 ng/mL EGF. Scale bar: 10 µm.